Two-Kaon and Two-Proton Interferometry in 158 GeV/Nucleon Pb+Pb Collisions

DISSERTATION

Presented in Partial Fulfillment of the Requirements for

the Degree Doctor of Philosophy in the

Graduate School of The Ohio State University

By

Dennis M. Reichhold, B.S., M.Eng.

* * * * *

The Ohio State University

2001

Dissertation Committee:

Dr. Thomas J. Humanic, Adviser

Dr. Evan R. Sugarbaker

Dr. Richard J. Furnstahl

Dr. Klaus Honscheid

Approved by

Adviser
Department of Physics

ABSTRACT

Kaon and proton interferometry measurements are made for the reactions Pb+Pb→ $K^+K^+ + X$ and Pb+Pb→ $pp + X$ using the 158 GeV/nucleon ^{208}Pb beam from the CERN Super Proton Synchrotron (SPS).

Two-particle intensity interferometry measurements are sensitive to the spatial and temporal extent of the source as well as the expansion dynamics of the system.

The focussing spectrometer experiment NA44 is used to detect the position and momentum coordinates of kaons and protons. NA44 has a narrow experimental acceptance that lies near mid-rapidity; for these measurements, the 131mr angular setting was used, with a mean transverse momentum of 910 MeV/c. Two-particle Coulomb corrections and experimental acceptance corrections are applied to the kaon data, which are fit to one- and two-dimensional Gaussian functions in momentum space to obtain radius parameters. Because proton correlations cannot be fit to analytic functions, different methods are used to extract radius parameters from the proton data.

ACKNOWLEDGMENTS

Many people played important roles in getting me as far as I have come. I wish to thank everyone who was ever a part of NA44, those I worked with, those I met, and those I never even saw.

Special thanks to Sanjeev Pandey for getting me started, and Dave Hardtke for keeping me going; to John Sullivan for helping me to understand HBT; to Ian Bearden for helping me to understand the experiment; to Allan Hansen for preventing us from killing each other. Thanks must also be extended to Hiroaki Ohnishi for solving the problems that no one thought had solutions and to Takeshi Kohama for finding the answers for which no one else found the time. No NA44 thesis would be complete without thanking Achim Franz. I would also like to thank Hans Bøggild, Hubert van Hecke, Michael Murray, Barbara Jacak, Jerry Dodd, Atsushi Sakagushi, Masashi Kaneta, Petra Hummel, Peter Christiansen, Janus Schmidt-Sorensen and the late Kevin Wolf. I would like to make special mention of the contributions of the late Kazuhiro Kaimi.

Of course, I must thank Tom Humanic, my adviser, for understanding how to keep me motivated without making me feel overly pressured.

I would also like to thank everyone at the Van de Graaff: Evan Sugarbaker, Michael Lisa, Gaspare LoCurto, Dan Cooper, Randy Wells, Bob Willson, Ivan Kotov, Helen Caines, Alex Murphy, Howard Dyke, Linda O'Brien, and Mary Smith.

Finally, I extend a heartfelt thanks to all my friends and family, extended as it is, who have supported me through the years, but especially to my parents for their love and for always pushing me to do my best.

VITA

May 19, 1969	Born - Port Jefferson, NY
1991	B.S. Applied and Engineering Physics Cornell University Ithaca, NY
1991-1992, 1994	Graduate Teaching Assistant Department of Applied and Engineering Physics Cornell University Ithaca, NY
1994	M.Eng. (Engineering Physics) Cornell University Ithaca, NY
1994-1995	Graduate Teaching Assistant Department of Physics The Ohio State University Columbus, OH
1995-1996	Graduate Exchange Student Rheinische Friedrich-Wilhelms- Universität Bonn Bonn, BRD
1996-1999	Graduate Research Assistant Department of Physics The Ohio State University Columbus, OH
1999-present	Post-doctoral Research Assistant Department of Physics Creighton University Omaha, NE

PUBLICATIONS

Collective Expansion in High Energy Heavy Ion Collisions, I.G. Bearden, *et al.*, Phys. Rev. Lett. **78**, 2080 (1997).

Particle Ratios from Central Pb+Pb Collisions at the CERN SPS, M. Kaneta, *et al.*, J. Phys. **G23**, 1865 (1997).

High Energy Pb+Pb Collisions Viewed by Pion Interferometry, I.G. Bearden, *et al.*, Phys. Rev. **C58**, 1656 (1998).

One-Particle, Two-Particle, and Three-Particle Hadron Spectra: Recent Results from CERN/SPS Experiment NA44, I.G. Bearden, *et al.*, Nucl. Phys. **A638**, 103c (1998).

Kaon and Proton Ratios from Central Pb+Pb Collisions at the CERN SPS, I.G. Bearden, *et al.*, Nucl. Phys. **A638**, 419c (1998).

Anti-deuteron and Kaon Production in Pb+Pb Collisions, I.G. Bearden, *et al.*, Nucl. Phys. **A661**, 55c (1999).

Deuteron and Triton Production in Pb+Pb Collisions at 158 AGeV, I.G. Bearden, *et al.*, Nucl. Phys. **A661**, 387c (1999).

Two Kaon Correlations from Pb+Pb Collisions at 160 AGeV from NA44, I.G. Bearden, *et al.*, Nucl. Phys. **A661**, 435c (1999).

Coalescence, Interferometry and Flow, I.G. Bearden, *et al.*, Nucl. Phys. **A661**, 456c (1999).

Strange Meson Enhancement in PbPb Collisions, I. Bearden, *et al.*, Phys. Lett. **B471** 6 (1999).

Antideuteron Production in 158A GeV/c Pb+Pb Collisions, I.G. Bearden, *et al.*, Phys. Rev. Lett. **85** 2681 (2000).

Elliptic Flow in Au+Au Collisions at (S(NN))(1/2) = 130 GeV**, K.H. Ackermann, *et al.*, Phys. Rev. Lett. **86** 402 (2001).

FIELDS OF STUDY

Major Field: Physics

TABLE OF CONTENTS

Page

Abstract ii

Acknowledgments iii

Vita v

List of Figures x

List of Tables xii

Chapters:

1. INTRODUCTION 1

2. THEORY OF INTENSITY INTERFEROMETRY 4

   2.1 Basics of Intensity Interferometry 4
   2.2 Final-State Interactions 8
      2.2.1 Strong Interaction 8
      2.2.2 Coulomb Interaction 9
   2.3 Parameterization of the Correlation Function 10
      2.3.1 One-Dimensional Parameterization 11
      2.3.2 Higher-Dimensional Parametrization 13
   2.4 LCMS Reference Frame 15

3. EXPERIMENT NA44 16

   3.1 The Target Area 18
   3.2 The Magnets 19
   3.3 The Detectors 22

3.3.1 The Hodoscopes 22
3.3.2 Multi-wire Proportional Chambers 23
3.3.3 Threshold Cerenkov Counters 24
3.3.4 Other Detectors 24
3.4 NA44 Monte-Carlo 25

4. DATA ANALYSIS 28

4.1 The Data 28
4.2 Hodoscope Calibrations 29
4.3 Reconstruction and DST production 30
4.4 Pair Files 32
4.5 Forming the Correlation Function 33
4.5.1 Coulomb Correction 35
4.5.2 Acceptance Correction 36
4.5.3 Background Correction 39
4.5.4 Fully Corrected Correlation Function 40
4.6 Fitting the Correlation Function 40

5. EXPERIMENTAL RESULTS AND DISCUSSION 43

5.1 One-Dimensional K^+K^+ Correlation Functions 43
5.2 Two-Dimensional K^+K^+ Correlation Functions 46
5.3 One-Dimensional *pp* Correlation Functions 49
5.4 Comparison with Other Pb+Pb Interferometry Data 51
5.5 Comparison to NA44 S+Pb Results 53
5.6 Comparison with a Rescattering Model 55

6. CONCLUSIONS 58

Appendices:

A. KINEMATIC VARIABLES 60

B. SYSTEMATIC ERRORS 62

Bibliography 65

LIST OF FIGURES

Figure **Page**

1.1 The theoretically predicted phase diagram for nuclear matter. 2

1.2 The theoretically predicted space-time evolution of a relativistic nuclear collision. 3

2.1 Schematic diagram for an HBT experiment. 6

2.2 Ideal correlation functions for kaons (solid) and protons (dashed). . . 12

2.3 A more realistic correlation function for protons. 13

2.4 The Bertsch-Pratt coordinate system used for 3-dimensional HBT analysis. 14

3.1 Experiment NA44 in 1996. 17

3.2 NA44 acceptance for kaons and protons in the 8 GeV/c high angle setting. 20

3.3 NA44 acceptance for 131mr protons (first graph) and kaons. 21

3.4 A comparison of data and MC for 8 GeV/c kaons in the 131mr horizontal setting. The solid lines are data and dashed lines are MC. . . . 27

4.1 H3 mass squared distributions for the 131mr 8 GeV/c horizontal setting. The upper plot shows the distribution with events where more than 220 ADC channels in C1 fired, and the lower plot has no cut on C1. Also shown are the expected positions for the kaon and proton peaks. 34

4.2 The ideal MC correlation function ($C_2(ideal)$), reconstructed MC correlation function ($C_2(reconstructed)$) and acceptance correction for kaons. The Bose-Einstein weights for each pair are calculated using $R_{inv} = 2.8$ fm and $\lambda = 0.4$. 38

5.1 The kaon correlation function in Q_{inv}, with the full Coulomb wave correction. The solid line is the fit function. 44

5.2 A comparison of the Coulomb Wave and Gamow corrections in Q_{inv}. 45

5.3 The 2d projections of the full Coulomb corrected correlation function using the standard Bertsch-Pratt parameterization. 47

5.4 A comparison between the two different correction methods for a fit in two dimensions. 48

5.5 The raw correlation function for protons. Note that $q_{inv} = \frac{1}{2}Q_{inv}$. . . 50

5.6 Output from the CRAB program for input Gaussian radii of 2.5 and 4.0 fm. 50

5.7 A comparison of the measured *pp* correlation function with the output from CRAB using a Gaussian source with R = 3.42 fm. 51

5.8 The radius parameters plotted with respect to m_t. The closed points are pion data, and the open points are kaon data, except the labeled proton point. The curve is the best fit to $R_L = Am_t^{-B}$, where A and B are fit parameters. 55

LIST OF TABLES

Table **Page**

3.1 The momentum resolution (in MeV/c) as calculated from the Monte-Carlo for Q_{inv}, Q_T, and Q_L for the 131mr 8 GeV/c horizontal setting. The Q_L resolution is evaluated in the LCMS frame. 26

5.1 Fitted results of Gaussian parameterizations of the correlation function in Q_{inv}. The errors are statistical $\pm$ systematic. 45

5.2 Fitted results of the two-dimensional Gaussian parameterization of the correlation function with both the Coulomb wave and Gamow corrections. Errors are statistical $\pm$ systematic. 49

5.3 One- and three-dimensional results from other NA44 analyses. The spectrometer setting for the kaon data was 6GeV; for the pions it was 4GeV. Errors are statistical $\pm$ systematic for kaons, statistical+systematic for pions. 52

5.4 Mean p_t and m_t for the different meson analyses. 53

5.5 One- and three-dimensional K^+K^+ results from NA44's S+Pb data. Errors are statistical $\pm$ systematic. 54

5.6 Results from a three-dimensional fit to a K^+K^+ correlation function using output from the rescattering model, and the NA44 two-dimensional results. 57

B.1 The standard HBT cuts and the variations used in the systematic error analysis. The meaning of each cut is explained in the text. Note that only MINCNT and bin size had different values between 1-d and 2-d. 63

B.2 Fitted 1-d and 2-d results for K^+K^+ correlation functions with the variations from Table B.1. The full Coulomb wave correction has been applied to these results. Errors are purely statistical. 64

B.3 The relative error from each source, and the total systematic error. . 64

CHAPTER 1

INTRODUCTION

The study of ultra-relativistic heavy-ion reactions brought together the two fields of high energy physics and nuclear physics. The primary difference between these two areas lies in their treatment of the strong nuclear force. High energy physics describes the strong force in terms of elementary particles (quarks) interacting through the exchange of gauge bosons (gluons). In the lower energy regime of nuclear physics, the direct quark-gluon interactions are shielded due to confinement, so the strong interaction is characterized by large composite particles (nucleons) exchanging smaller composite particles (mesons). Relativistic heavy-ion physics attempts to describe the intermediate region, where the nuclear is subjected to conditions of extreme temperature and baryon density.

Under "normal" conditions (e.g., a block of lead at 290 K), quarks are confined to nucleons, which in turn are confined to nuclei (see Figure 1.1). Increasing the temperature or baryon density would cause nuclei to deconfine, forming a hadron gas of nucleons (protons and neutrons) and other baryons (e.g., Λ) and mesons (e.g., π and K). Further heating or compressing would cause the hadrons themselves to deconfine, leaving a system of quarks and gluons, the quark-gluon plasma (QGP). Both lattice quantum-chromodynamics (QCD) and the MIT bag model make predictions as to the

existence of the QGP, a phase of matter which has yet to be observed, but is believed to have existed in the universe less than one microsecond after the Big Bang.

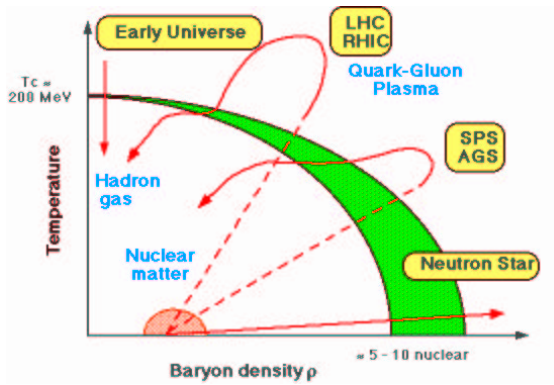

Figure 1.1: The theoretically predicted phase diagram for nuclear matter.

In the laboratory, relativistic nucleus-nucleus collisions provide the best opportunity for recreating the conditions of a QGP. The time evolution of a collision in which a QGP is created is shown in Figure 1.2. The time between the collision and the hadronic freeze-out is on the order of a few fm/c ($10^{-23}s$), so the direct detection of a QGP is virtually impossible. Freeze-out is defined as the point after which the hadrons no longer interact strongly with each other. Since experiments can only detect hadrons after freeze-out, theoretical models must be used to interpolate backwards in time.

The goal of this thesis is to use intensity interferometry of identical hadrons to study the spatial and temporal extent of the most energetic fixed-target heavy-ion collisions, Pb+Pb collisions at 158 GeV/nucleon. Specifically, results from kaon-kaon (KK) and proton-proton (pp) correlations will be presented and compared with

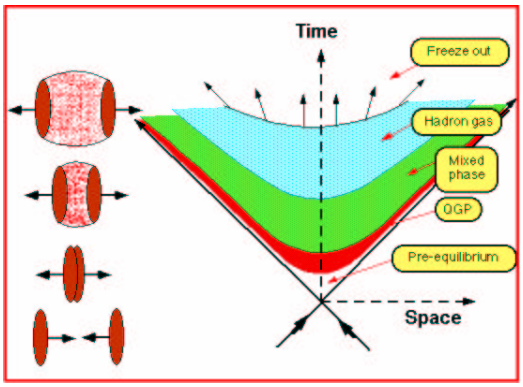

Figure 1.2: The theoretically predicted space-time evolution of a relativistic nuclear collision.

results from pion-pion ($\pi\pi$) interferometry, the most commonly studied type of correlation. Comparisons to models will also be made.

CHAPTER 2

THEORY OF INTENSITY INTERFEROMETRY

In the 1950's, Hanbury-Brown and Twiss became the first to use the technique of intensity interferometry to measure the angular sizes of distant stars (the technique was subsequently named Hanbury-Brown-Twiss interferometry, or HBT) [HBT56]. A few years later, Goldhaber, Goldhaber, Lee and Pais applied the same technique (though independently developed) to pion pairs emitted from proton-antiproton collisions [GGLP60].

When HBT was first used in heavy-ion collisions, it was thought that the extracted numbers were the radii of the source. It is now understood that HBT does not directly probe the collision fireball (as no hadronic observable can). However, HBT measurements, as well as other hadronic measurements from ultra-relativistic heavy ion collisions, do probe the state of the system at freeze-out, providing a set of observables which can be compared with, and thus validate, different theoretical models.

2.1 Basics of Intensity Interferometry

Intensity interferometry, as its name implies, compares the intensity of two or more particle wave functions, as opposed to amplitude interferometry, such as the

double slit experiment in optics. While amplitude interferometry can only be used when the source is coherent, HBT is only meaningful with an *incoherent* source.

Imagine a source with density distribution function $\rho(\vec{r})$, emitting two identical particles $\vec{r}_1$ and $\vec{r}_2$, as shown in Figure 2.1. Some detectors at points A and B measure these particles' momenta as $\vec{p}_1$ and $\vec{p}_2$. It cannot be determined which particle originated from which position. Treating the particles as plane waves, the wave-function describing these two particles can be written as:

$$\Psi_{12}(\vec{r}_1, \vec{r}_2) = \frac{1}{\sqrt{2}}(e^{i\vec{p}_1\vec{r}_1}e^{i\vec{p}_2\vec{r}_2} \pm e^{i\vec{p}_1\vec{r}_2}e^{i\vec{p}_2\vec{r}_1})|+> + \frac{1}{\sqrt{2}}(e^{i\vec{p}_1\vec{r}_1}e^{i\vec{p}_2\vec{r}_2} \mp e^{i\vec{p}_1\vec{r}_2}e^{i\vec{p}_2\vec{r}_1})|->. \quad (2.1)$$

In this equation, the upper signs are for bosons, while the lower signs are for fermions. The $|\pm>$ are kets representing the sum of all symmetric ($|+>$) or anti-symmetric ($|->$) spin states. In the simplest case, spinless bosons (e.g., pions and kaons), $|->$ is identically zero, and $|+>=|00>$. For spin-$\frac{1}{2}$ fermions (e.g., protons and neutrons):

$$|+> \;=\; \frac{1}{2}(|\uparrow\uparrow> + \frac{1}{\sqrt{2}}(|\uparrow\downarrow> + |\downarrow\uparrow>) + |\downarrow\downarrow>), \textit{and} \quad (2.2)$$

$$|-> \;=\; \frac{1}{2\sqrt{2}}(|\uparrow\downarrow> - |\downarrow\uparrow>). \quad (2.3)$$

Since these kets make the anti-symmetric and symmetric spatial parts orthogonal, one can drop one of the terms for the following discussion without loss of generality, i.e.,

$$\Psi_{12}(\vec{r}_1, \vec{r}_2) = \frac{1}{\sqrt{2}}(e^{i\vec{p}_1\vec{r}_1}e^{i\vec{p}_2\vec{r}_2} \pm e^{i\vec{p}_1\vec{r}_2}e^{i\vec{p}_2\vec{r}_1}). \quad (2.4)$$

The probability for detecting these two particles is given by [BGJ90]:

$$P_C(\vec{p}_1, \vec{p}_2) = \frac{1}{2}|\int d^3r_1 d^3r_2 \Psi_{12}(\vec{r}_1, \vec{r}_2)\rho(\vec{r}_1)\rho(\vec{r}_2)|^2. \quad (2.5)$$

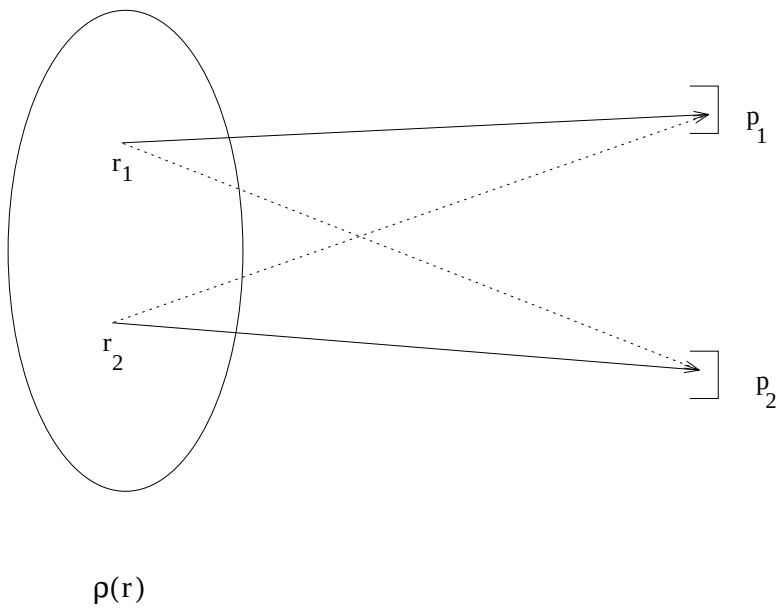

Figure 2.1: Schematic diagram for an HBT experiment.

Assuming a coherent source, this expression vanishes if the spatial portion of the wave function is anti-symmetric. For a symmetric spatial wave function, it reduces to:

$$P_C(\vec{p}_1, \vec{p}_2) \quad = \quad |\tilde{\rho}(\vec{p}_1)\tilde{\rho}(\vec{p}_2)|^2, \tag{2.6}$$

the square of the product of two Fourier transforms of the source amplitude function. This can be further reduced to;

$$P_C(\vec{p}_1, \vec{p}_2) \quad = \quad |\tilde{\rho}(\vec{p}_1)|^2|\tilde{\rho}(\vec{p}_2)|^2, \tag{2.7}$$

which is the product of the probability for detecting single particles with momenta, $\vec{p}_1$ and $\vec{p}_2$. So there would be no correlation between the two particles in this case [GKW79].

If the source is incoherent, then the probability of detecting the two particles becomes:

$$P_C(\vec{p}_1, \vec{p}_2) = 1 \pm |\tilde{\rho}(\vec{Q})|^2, \tag{2.8}$$

where $\vec{Q}$ is the difference between the two particles' momenta. With the spin wave functions, the probability becomes:

$$P_C(\vec{p}_1, \vec{p}_2) = 1 \pm (< +|+ > - < -|- >)|\tilde{\rho}(\vec{Q})|^2 \tag{2.9}$$

So, for spinless bosons, the joint probability is:

$$P_C(\vec{p}_1, \vec{p}_2) \;=\; 1 + |\tilde{\rho}(\vec{Q})|^2, \tag{2.10}$$

and for spin-$\frac{1}{2}$ fermions:

$$P_C(\vec{p}_1, \vec{p}_2) \;=\; 1 + (\frac{1}{4} - \frac{3}{4})|\tilde{\rho}(\vec{Q})|^2 \tag{2.11}$$

$$\;=\; 1 - \frac{1}{2}|\tilde{\rho}(\vec{Q})|^2. \tag{2.12}$$

The correlation function is defined as this joint probability function:

$$C_2(\vec{Q}) \;\equiv\; P_C(\vec{p}_1, \vec{p}_2). \tag{2.13}$$

So the correlation function provides a way to measure the square of the Fourier transform of the source density distribution function.

This derivation has assumed that the source had a constant distribution function with respect to time, an invalid assumption for heavy ion collisions given the extremely short lifetime of the source. It has also been assumed that there are no correlations between a particle's momentum and the position from which it was emitted. A further invalid assumption is that the only interaction between these particles arises

from quantum mechanical statistics; that is, once the particles have been emitted from the source, they no longer interact with each other.

In the case of an expanding system, the correlation function is not dependent solely on the momentum difference [Pra84, Pra86]. A moving region of the source is more likely to produce particles moving with a velocity comparable to that region. Because of this, the correlation function will also depend on the average momentum of the pair, $\vec{K} = \frac{1}{2}(\vec{p}_1 + \vec{p}_2)$. As a result, the size of a source distribution cannot be measured directly through interferometry. However, information about the dynamics of the source can be extracted using a correlation that is a function of both the momentum difference and total momentum of the pair of particles.

2.2 Final-State Interactions

The derivation thus far has assumed that the only interaction between the particles is quantum mechanical statistics. All the hadrons emitted from a heavy ion collision interact with each other via the strong force. Furthermore, if the particles are charged, they will exert a Coulomb force on each other. For charged pions and kaons, these interactions affect the shape of the correlation function, but for protons, these interactions determine the shape. Since the actual measurements would take place after these interactions, their effects should be taken into account.

2.2.1 Strong Interaction

Bowler [Bow88] has studied the strong interaction between pions, and it is reasonable to assume that the results would be similar for kaons. His estimation is that the

repulsive force between two pions has a range of approximately 0.2 fm. The characteristic separation of kaons would be on the order of 1 fm, so this force can essentially be ignored.

For protons, the strong force is much more significant. At short range, there is an attractive s-wave potential, approximated by the Reid soft core potential [Rei68]. This attraction leads to a peak in the correlation function near $Q_{inv} \simeq 40$ MeV/c and dominates all other effects in defining the shape of the correlation function [Koo77]. Because of the symmetry of the s-wave, the correlation function depends only on the volume of the source, so for pp correlations, only a one-dimensional parametrization is necessary.

2.2.2 Coulomb Interaction

For both protons and charged kaons, the Coulomb interaction has a much larger range. With like-sign charged particles, this force is repulsive, and significantly suppresses the two-particle probability at low relative momentum.

It has long been established [Sch68] that the Coulomb potential between two like-signed particles will affect the solution to Schrödinger equation according to the Gamow factor:

$$G(\eta) = \frac{2\pi\eta}{e^{2\pi\eta} - 1}, \tag{2.14}$$

where $\eta = me^2/Q$, with m the mass of the particle, and e the charge. A more detailed study of this effect on HBT analysis was performed by Gyulassy, *et al.* [GKW79]. Later, Pratt [Pra86b] developed a formalism that did not assume a point-like source, yielding a complicated integral that must be calculated numerically:

$$P(\vec{p}_1, \vec{p}_2) = \int d^3r_1 d^3r_2 |e^{i(\vec{p}_1+\vec{p}_2)\cdot(\vec{r}_1+\vec{r}_2)/2} \times \psi_r(\Delta\vec{p}, \Delta\vec{r})|^2 \rho(\vec{r}_1)\rho(\vec{r}_2), \tag{2.15}$$

where ψ_r is a symmetrized wave function:

$$\psi_r(\vec{Q},\vec{r}) = \frac{1}{\sqrt{2}}(\psi_c(\vec{Q},\vec{r}) + \psi_c(\vec{Q},-\vec{r})), \tag{2.16}$$

obtained from the Coulomb wave function:

$$\psi_c(\vec{Q},\vec{r}) = \Gamma(1+i\eta)e^{-\pi\eta/2}e^{iQr}F(-i\eta;1;iQr - i\vec{Q}\cdot\vec{r}), \tag{2.17}$$

where F is a confluent hypergeometric function. Equation (2.15) can be used to correct real data, provided an analytic functional form for the correlation function has been assumed. In the case of boson interferometry, a Gaussian parametrization is used to iteratively calculate $\rho(\vec{r})$, using the correlation function from the previous iteration.

For fermion interferometry, the Coulomb interaction completely suppresses the correlation function at zero relative momentum. No analytic functional form is assumed for proton correlations, so these effects must be incorporated into any model used for comparison.

Naturally, the out-going particles will also experience a Coulomb interaction with the residual nuclear source. Due to the complicated three-body dynamics, this effect has been left out of most of the literature. A study was done using data from the Bevalac [Cha88], which showed that this interaction has an effect on the correlation function. However, for this study, it will be ignored.

2.3 Parameterization of the Correlation Function

Equation (2.9) is the general expression for a correlation function. Assuming that the original source density function, $\rho(\vec{r})$, is a Gaussian distribution, then its Fourier transform, $\tilde{\rho}(\vec{Q})$ will also be Gaussian. Barring final state interactions, the correlation

function would therefore also be Gaussian. To continue this discussion, a choice of reference frame and coordinate system is necessary.

2.3.1 One-Dimensional Parameterization

As mentioned in section 2.2.1, only a one-dimensional parametrization of the *pp* correlation function is necessary. If one wishes to compare HBT results from protons and kaons, then a 1-d correlation for KK should also be examined. A convenient choice is the Lorentz invariant momentum difference between the two particles:

$$Q_{inv} = \sqrt{|\vec{Q}|^2 - Q_0^2}, \tag{2.18}$$

where Q_0 is the difference in the two particles' energies. With this parametrization, the correlation function is:

$$C_2(Q_{inv}) = 1 + \lambda e^{-Q_{inv}^2 R_{inv}^2}, \tag{2.19}$$

where R_{inv} is the invariant radius parameter, and λ is a parameter that depends on the particles under study.

Barring final state interactions, ideal one-dimensional correlation functions are shown in Figure 2.2. The solid line depicts an ideal function for kaons (or any other spinless bosons), and the dashed line shows an ideal proton (or other spin-$\frac{1}{2}$ fermion) correlation.

A "true" *pp* correlation function from a Pb+Pb collision would look more like 2.3. This figure shows the suppression at $Q_{inv} = 0$ due to the Coulomb interaction, and the peak near $Q_{inv} \simeq 40$ MeV/c. The height of the peak is inversely proportional to perceived size of the source [Koo77]. In order to extract a radius, a measured correlation function must be compared with the correlation function from simulated data where the source size is known.

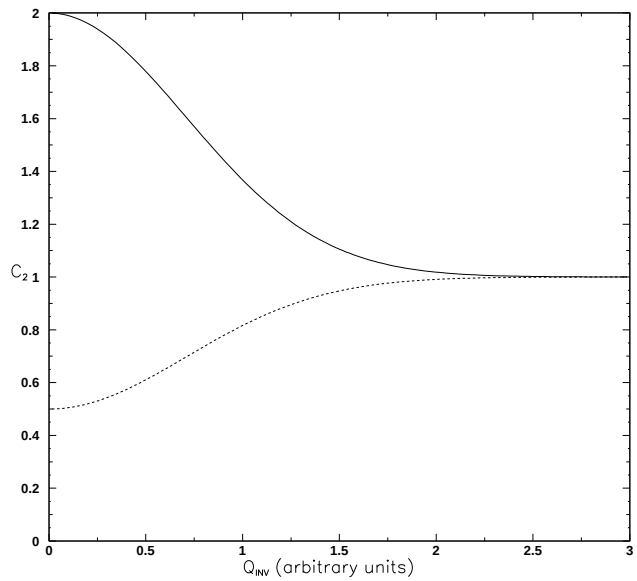

Figure 2.2: Ideal correlation functions for kaons (solid) and protons (dashed).

With bosons, the correlation function will also experience distortions. For a completely incoherent source, λ will be equal to unity, and for a completely coherent source, it will vanish [GKW79]. Therefore, λ is a measure for the degree of coherence of the source. For this reason, it is referred to as the chaoticity parameter.

Using Q_{inv} has the advantage of not depending on reference frame, which simplifies comparison between two different experiments. This parametrization also requires fewer statistics, so if an experiment has a limited number of identical particle pairs, a one-dimensional parametrization could still be possible. The disadvantage, as pointed out by Bowler [Bow85], is that R_{inv} probes an average over the four-vector Q, so information of the full spatial extent of the source is lost.

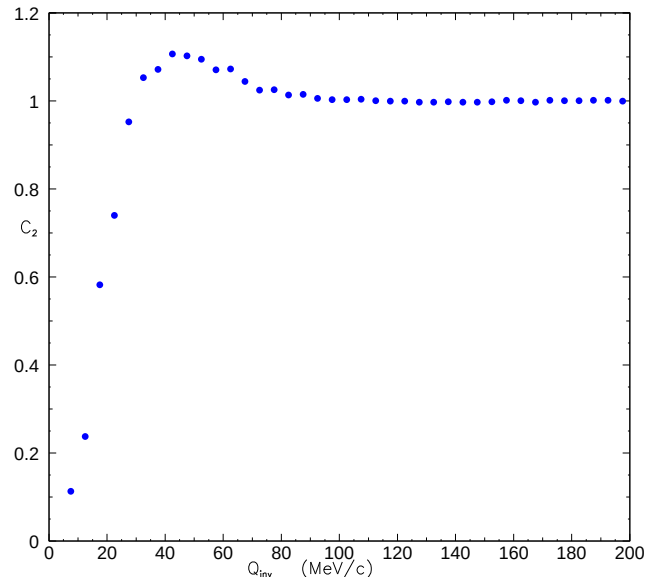

Figure 2.3: A more realistic correlation function for protons.

2.3.2 Higher-Dimensional Parametrization

Given ample statistics and an appropriate experimental acceptance, a more complete parametrization is possible. The three-dimensional parametrization most commonly used is the Bertsch-Pratt coordinate system [BGT88, Pra86]. The momentum difference $\vec{Q}$ is broken down into Q_L and Q_T. Q_L, the "longitudinal" direction, is parallel to the beam direction, and Q_T is transverse. In a two-dimensional parametrization, these are the coordinates used. For 3-d, Q_T, or more appropriately, $\vec{Q_T}$ is further broken down. The outward direction is defined as parallel to the total transverse momentum of the pair, and the sideward direction is perpendicular to that. So the

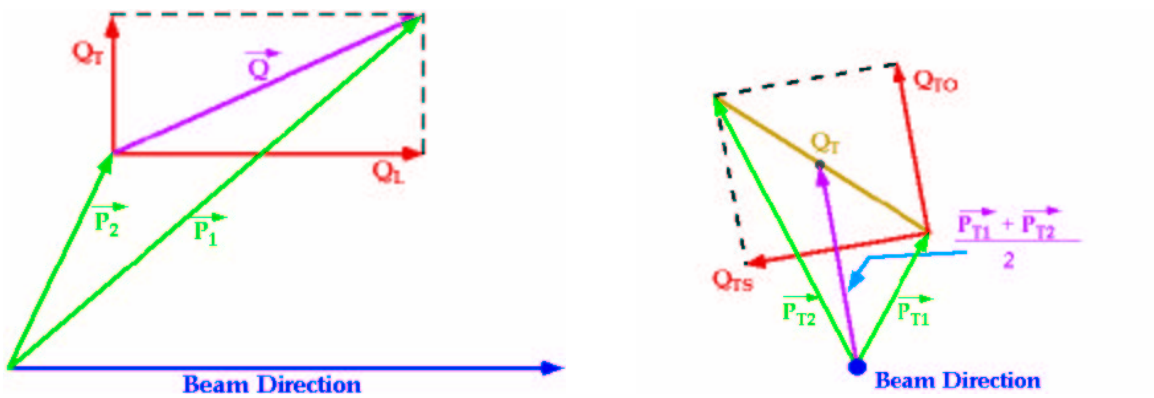

Figure 2.4: The Bertsch-Pratt coordinate system used for 3-dimensional HBT analysis.

momentum difference $\vec{Q}$ would be represented as (Q_{TO}, Q_{TS}, Q_L), as illustrated in Figure 2.4.

Using these coordinates, the two-dimensional Gaussian correlation function is:

$$C_2(\vec{Q}) = 1 + \lambda e^{-Q_T^2 R_T^2 - Q_L^2 R_L^2}, \tag{2.20}$$

and in three dimensions:

$$C_2(\vec{Q}) = 1 + \lambda e^{-Q_{TO}^2 R_{TO}^2 - Q_{TS}^2 R_{TS}^2 - Q_L^2 R_L^2}. \tag{2.21}$$

These radius parameters are referred to as longitudinal (R_L), transverse (R_T), outward (R_{TO}), and sideward (R_{TS}).

As the focus of this work is on two-dimensional analysis, no more will be said about the three-dimensional parametrization. For a more detailed study of the implications of a three-dimensional analysis, see [Har97].

2.4 LCMS Reference Frame

Once the coordinate system has been decided upon, the reference frame must be chosen. For this study, the longitudinally co-moving system (LCMS), suggested by Pratt [PCZ90], will be used. In this frame, the total momentum of the pair is in the transverse direction:

$$p_{z_1} + p_{z_2} = 0, \tag{2.22}$$

where p_{z_i} is the momentum of the ith along the direction of the beam, the z-direction. It should be pointed out that both the reference frame and the coordinate system are different for each pair.

CHAPTER 3

EXPERIMENT NA44

The heavy-ion experiment NA44 sat in CERN's North Experimental Hall in Prevessin, France, just across the border from Geneva, Switzerland. A second-generation, fixed-target experiment, it was originally designed to use the Super Proton Synchrotron's (SPS) 200 GeV/nucleon ^{32}S beam from the H4 beamline. When the SPS was upgraded in 1994 to inject a 158 GeV/nucleon ^{208}Pb beam, NA44 was also upgraded. The Pb beam was used from 1994 until the experiment was de-commisioned, in 1996. For the Pb ions, the maximum beam intensity was 6×10^6 particles per spill, and each spill lasted 2 seconds; for the data here, the beam intensity was closer to 3×10^6 Pb ions per spill.

NA44 is a focussing spectrometer that specializes in the detection of a few particles near mid-rapidity, meaning single-particle yields and spectra and two- and three-particle correlations were typically studied. Figure 3.1 shows the experiment as it was during the 1996 Pb run. NA44 had a small acceptance, so only a few particles per event were detected. As a result, the detector had excellent particle identification (PID) on a track-by-track basis. Both Cerenkov detectors and time-of-flight measurements were used in PID.

The entire detector was mounted on movable supports to increase the range in transverse momentum (p_t) that could be studied. The spectrometer could be positioned at two different angles: 44mr (2°) and 131mr (7°), or small angle and large angle.

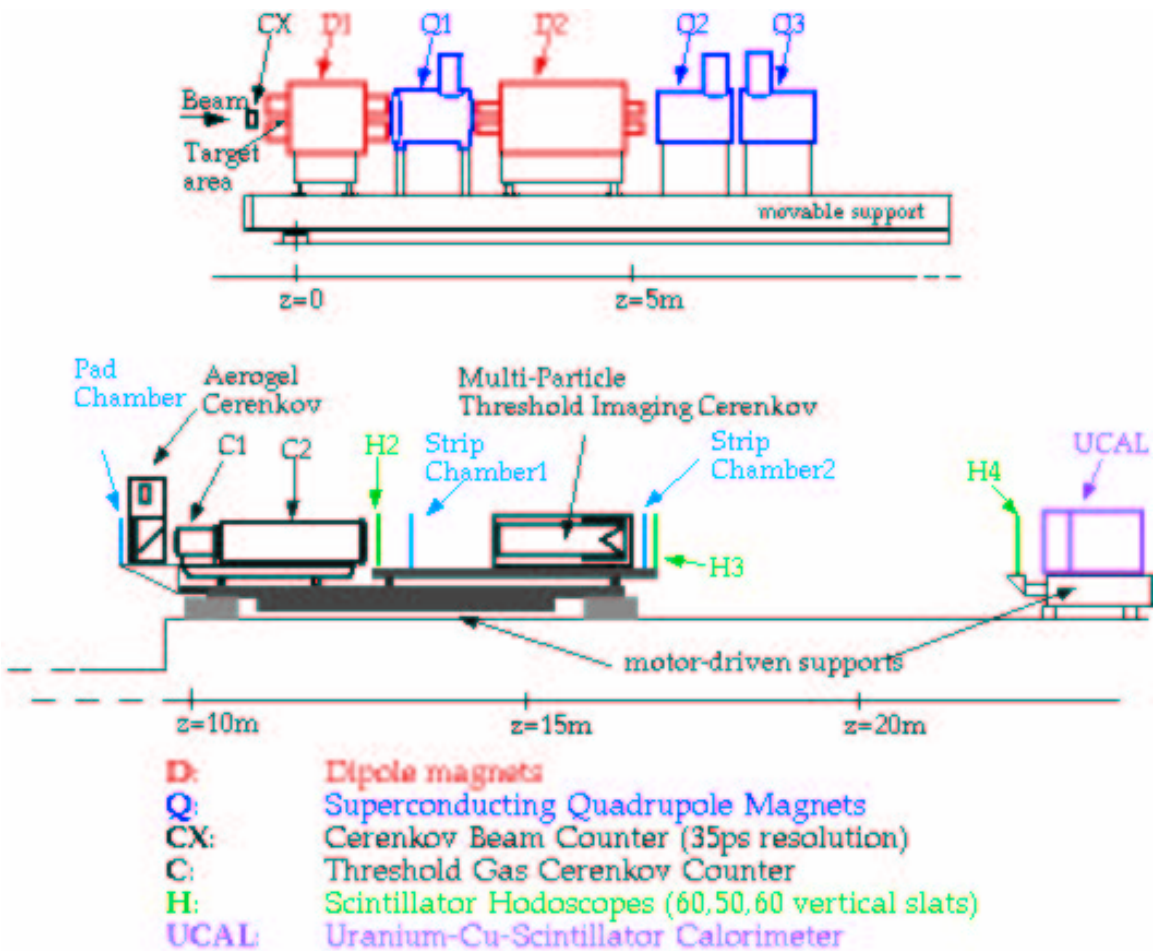

Figure 3.1: Experiment NA44 in 1996.

3.1 The Target Area

Upstream of the target, two detectors are used to ensure a "clean" beam is striking the target. The first is a Cerenkov beam counter, consisting of two phototubes, each connected to a Cerenkov chamber. These detectors are used to estimate the timing resolution and to eliminate events with a "double beam." A double beam occurs when more than one beam particle strikes the target within the limit of the detector's time resolution.

Two scintillators, CXVLA and CXVRA, are located around the beam line. A large signal in either of hese detecors indicates that the beam is off-target; a large signal in both these detectors would be indicative of a "beam-halo." In either case, the beam would be less likely to hit the target than some surrounding material. Events with such large signals are always rejected.

The target sat just downstream of the beam counter and CX. For the data presented here, a Pb target of 6 mm thickness was used.

Downstream of the target sat two centrality detectors, T0 and a silicon pad detector. The two thin pieces of scintillator that make up T0 are placed far enough apart that any particle within NA44's acceptance window would pass between them. Other particles produced from the collision within the psuedo-rapidity range $1.3 \leq \eta \leq 3.5$ would hit the scintillators. Each scintillator was attached to two phototubes. Assuming particle multiplicity to be proportional to centrality, the analog-to-digital-converter (ADC) signals from T0 were used as the centrality trigger. The estimate on centrality from T0 came from:

$$\text{centrality} \approx \frac{\text{T0 count rate}}{\text{beam counter rate} \times \text{target interaction length}}. \tag{3.1}$$

The electrons not completely removed from the Pb ion beam, called delta electrons, formed a large percentage of the particles detected by T0. These electrons were swept to one side by the first dipole magnet, in which T0 sat.

The silicon pad multiplicity detector consisted of 512 pads, and had full azimuthal symmetry in the pseudo-rapidity range $1 \leq \eta \leq 4$. It supplied an additional check of centrality in off-line analysis.

3.2 The Magnets

Figure 3.1 shows the magnets used in NA44: two dipoles (D1 and D2), and three superconducting quadrupoles (Q1, Q2, and Q3). The dipoles were used to select different nominal momenta of the particles being measured. The momenta typically selected were 4 GeV/c, 6 GeV/c, and 8 GeV/c, each $\pm \approx 20\%$.

The superconducting quadrupoles were used to focus the particles in a particular plane, either the horizontal or the vertical. Because each plane maximizes the acceptance of a different set of two of the three components of $\vec{Q}$, using the quadrupoles optimizes the spectrometer for HBT studies.

Selecting the horizontal setting would maximize the acceptance for Q_{TO} and Q_L; Q_{TS} and Q_{TO} are measured better with the vertical setting. Due to time constraints in the data taking, only one setting was possible for the data discussed in this thesis. The horizontal setting was selected because it has better momentum resolution [Har97]. NA44's acceptances for kaons and protons in the 8 GeV/c horizontal, large angle setting are shown in Figure 3.2 on a p_t versus rapidity plot. Figure 3.3 shows the acceptances for the relative momenta for both protons and kaons.

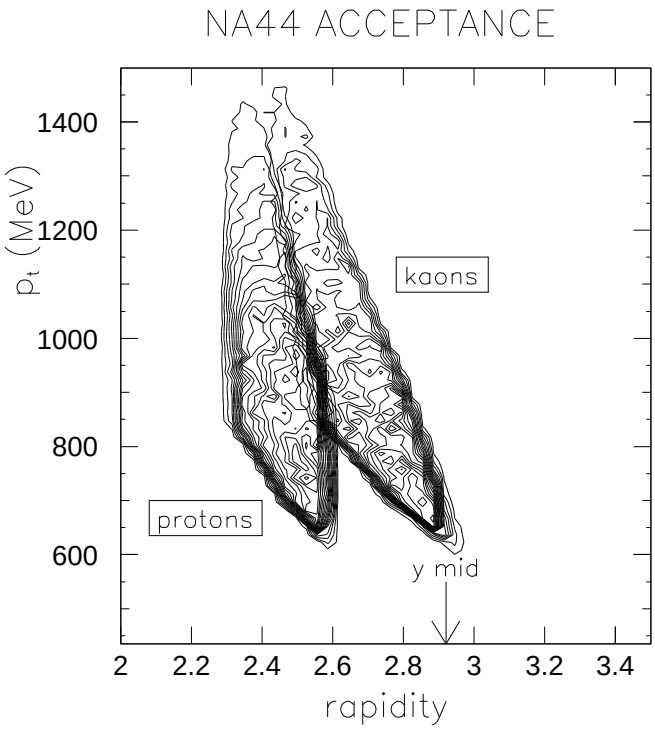

Figure 3.2: NA44 acceptance for kaons and protons in the 8 GeV/c high angle setting.

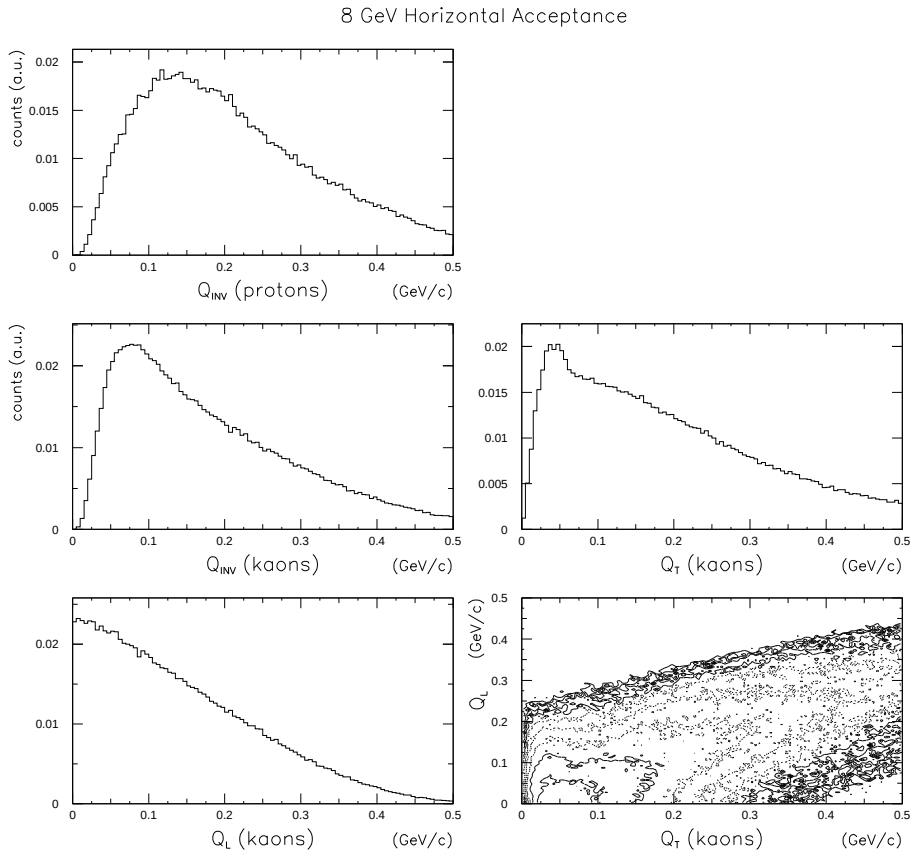

Figure 3.3: NA44 acceptance for 131mr protons (first graph) and kaons.

3.3 The Detectors

Downstream of the magnets sat the various detectors that made up the core of NA44. These detectors were used to identify particles and to track their trajectories. Three highly segmented, scintillating time-of-flight (TOF) hodoscopes and three multi-wire proportional chambers provided position and timing measurements that were used to calculate the momenta and velocities of the various particles. In addition, three Cerenkov detectors were used to identify the presence or absence of certain particles. There were other detectors in place, but they were not used for analyzing the data set described in this thesis.

3.3.1 The Hodoscopes

The three hodoscopes in NA44, H2, H3, and H4, were located, respectively, 13.9 m, 18.4 m, and 24.7 m from the target. H2 and H4 each had 60 vertically aligned slats of plastic scintillator; H3 had 50 slats. The slats on H2 were 6 mm wide by 6 mm thick by 200 mm long; on H3 they were $13 \times 10 \times 220$ mm; on H4 they were $23 \times 20 \times 700$ mm. While H2 and H3 sat perpendicular to the length of the experiment, H4 was at a slight angle, which varied with the angular setting of the spectrometer.

Each slat was attached at top and bottom to a photomultiplier tube. The y-position of a charged particle hitting a slat could be calculated using the time difference between light hitting the two phototubes. For H2, H3, and H4, the resolution in the y-direction was estimated to be 9, 7, and 13 mm. Since the x-position was determined by which slat the particle passed through, the x-resolution is the same as the width of the slat. The timing resolution for TOF in each hodoscope was approximately 100 ps. The time-to-digital-converter (TDC) signals from the hodoscopes

were used to trigger on events. An event was considered to be a valid "pair event" if there were at least two simultaneous hits in both H2 and H3.

Almost 35% of all 8 GeV/c kaons decayed before reaching H4, because it was located $.41c\tau$ from the target, in the kaons reference frame. Therefore, in the kaon analysis, H4 was only used as an additional check on the TOF; valid hits in H4 were not required for all kaon events.

3.3.2 Multi-wire Proportional Chambers

The three multi-wire proportional chambers in NA44 were the pad chamber (PC) and two strip chambers (SC1 and SC2). The PC, located 9.5 m downstream from the target, could simultaneously measure the x and y positions of a particle passing through, by nature of its pad readout. It had a y-resolution of 2.7 mm and an x-resolution of 4.3 mm. The information from the PC played a significant part in calculating the particle's momentum.

The two strip chambers were located in close proximity to H2 and H3. SC1 sat directly behind H2, at 14.4 m downstream of the target, and SC2 sat directly in front of H3, at 17.9 m downstream. Each detector had two sets of parallel strips, one set horizontal and the other vertical. In reconstructing tracks, each strip chamber was treated as two detectors; the vertical strips supplied the x-positions of each hit, and the horizontal strips supplied the y-positions. The x-resolution of SC1 was 1.2 mm, and the y-resolution was 1.1 mm; for SC2, the x-resolution was 1.4 mm, and the y-resolution was 2.3 mm.

For two-particle analysis, one has to be careful not to confuse one track for two. In order to avoid the creation of such "ghost tracks," cuts were applied to the data

such that tracks had separations of less than 5 mm in the pad chamber. A similar requirement was made on hits in the strip chambers. Furthermore, two nearby tracks in the hodoscopes had to have at least one slat between them.

3.3.3 Threshold Cerenkov Counters

C1 and C2 are two threshold Cerenkov counters used to trigger on the presence or absence of certain species of particles. Both detectors, lcated downstream of the pad chamber and before H2, were filled with gas that can be set to high or low pressure settings. A change in the pressure of the gas changed the index of refraction, which changed the minimum velocity, or threshold, needed for the emission of Cerenkov light.

The trigger was set to require, ignore, or reject (veto) events in which either Cerenkov fired. For these data, C2 was used to reject events with particles lighter than kaons (mostly pions or electrons), and C1 was used off-line to detect the presence of kaons. The trigger was set to veto events with C2, and ignore C1.

Further downstream, before SC2, sat another Cerenkov detector, the TIC (Threshold Imaging Cerenkov). This was used to positively identify pions on a track-by-track basis. Since most pions in this data sample were rejected by the C2 veto in the trigger, the TIC only served to eliminate a small number of events.

3.3.4 Other Detectors

Two other detectors not used in this analysis were also a part of NA44, an Aerogel Cerenkov counter, located between PC and C1, and a uranium calorimeter (UCAL), situated directly downstream from H4. Unfortunately, the aerogel detector never operated as well as expected, so it was not used in any analysis. The UCAL was

used in single particle analysis to eliminate electrons and muons from pion and kaon spectra, and it was also useful in anti-deuteron analysis.

3.4 NA44 Monte-Carlo

Due to the finite acceptance and momentum resolution of the NA44 experiment, an experimental bias was introduced into the data analysis. A Monte-Carlo simulation of the experiment was used to try to correct for these distortions. This program was based on the DECAY TURTLE (ref [Bro74]) and TRANSPORT (ref [Bro80]) simulation packages.

The first step of the Monte-Carlo code was to generate a momentum distribution of particles. This could be a distribution of one particle species, or a mix of several. The distribution used was a thermal one:

$$\frac{1}{m_t^2}\frac{d^2N}{dy\,dm_t} = e^{(-m_t/T)}e^{((y-y_0)^2/\sigma^2)} \tag{3.2}$$

Here, m_t is the transverse mass of the particle, y is the rapidity, T is the inverse slope parameter, and σ is the width of the rapidity distribution. The inverse slope parameter was taken from single particle analysis; σ was taken directly from rapidity distributions.

Given a distribution of momentum and position points, the Monte-Carlo code sends these tracks through a simulation of the spectrometer. These "measurements" are then reconstructed as if they were real data. The discrepancies between the initial and the reconstructed momenta can then be used to correct for any experimental bias.

A comparison between Monte-Carlo distributions and real data is shown in Figure 3.4. This is for 8 GeV/c, wide-angle kaons in the horizontal setting. The Monte-Carlo output agrees quite well with the data. Although there is a slight difference in

the distributions for the x confidence level (CLX), this difference is below the cut on CL, and is therefore not significant for this analysis.

The differences between the initial Monte-Carlo momenta and the reconstructed Monte-Carlo momenta can be used to roughly calculate NA44's momentum resolution. Assuming that the distribution of the differences is Gaussian, then the width of the distribution would be the resolution. Table 3.1 shows the momentum resolution for the high angle, 8 GeV/c, horizontal setting.

Momentum component	Resolution
$\sigma(\Delta Q_{inv})$	14.0
$\sigma(\Delta Q_T)$	15.4
$\sigma(\Delta Q_L)$	13.5

Table 3.1: The momentum resolution (in MeV/c) as calculated from the Monte-Carlo for Q_{inv}, Q_T, and Q_L for the 131mr 8 GeV/c horizontal setting. The Q_L resolution is evaluated in the LCMS frame.

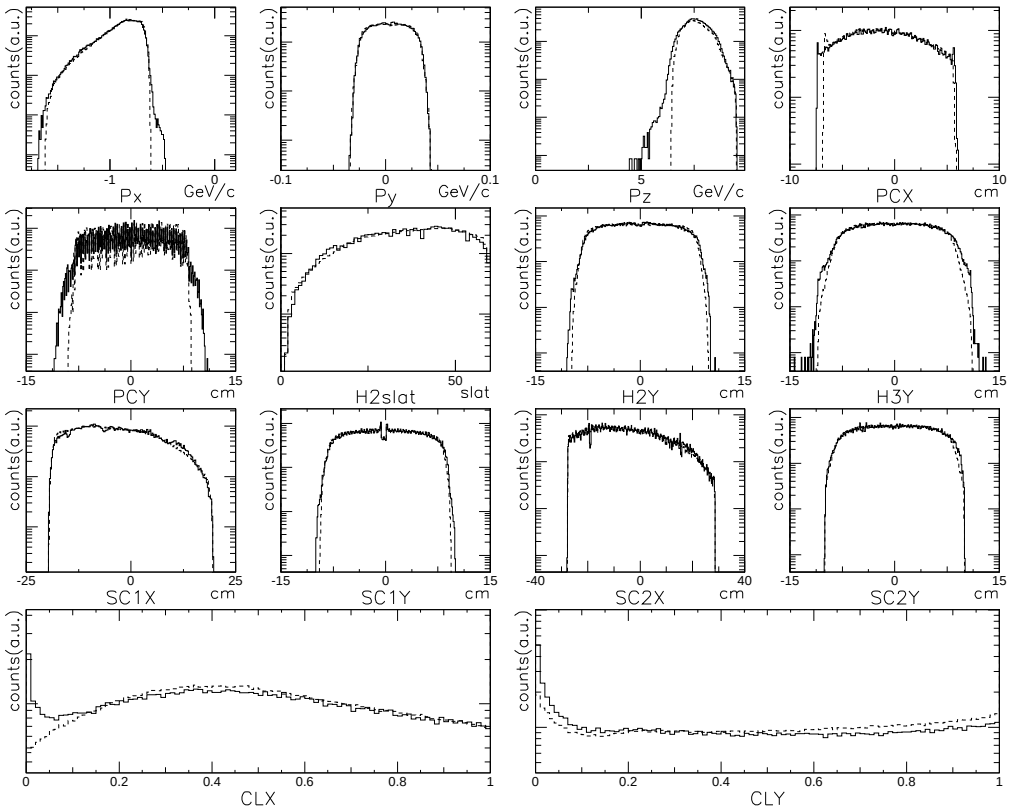

Figure 3.4: A comparison of data and MC for 8 GeV/c kaons in the 131mr horizontal setting. The solid lines are data and dashed lines are MC.

CHAPTER 4

DATA ANALYSIS

The goal of this chapter is to describe the reduction of NA44 measurements from raw data to files of momentum and position vectors, and the production of a correlation function from those files. The calibration of the main detectors and the reconstruction of tracks will be discussed. The selection of suitable particle pairs and the construction of the correlation function and its significance will also be presented.

4.1 The Data

All the data analyzed for this thesis were collected in the fall of 1996, with the spectrometer in the high angle, 8 GeV setting. The trigger was set for pairs of particles with a mass of the kaon or higher, so K^+K^+, K^+p, and pp were the most frequently accepted valid pairs. The results from the K^+K^+ analysis will be compared with a similar analysis performed by Takeshi Kohama at the University of Hiroshima on a low-p_t K^+K^+ sample taken during the 1995 Pb run.

Pions are the most abundantly produced particles in heavy ion collisions, with protons and kaons a distant second and third. As a result, there was a lot of dead time between accepted events. A total of 68 valid runs (run nos. 4677-4779) were taken over the period of a week, with each run containing approximately 35K events.

The limiting factor of each run is the amount of data that can be stored on an IBM 3250 magnetic tape; one tape contains one run. The target used was made of lead, with a thickness of 3.405 g/cm^2 (3 mm) which is on the order of 6.3% of an interaction length for a Pb projectile. The trigger centrality was set to $\sigma_{trig}/\sigma_{geom} = 19 \pm 1\%$.

4.2 Hodoscope Calibrations

In order to optimize the performance of the three hodoscopes and the CX counter, calibrations must be performed on a regular basis. Separate calibrating runs are not needed; the data are used directly. During an extended length of time with the same trigger settings, the detectors must be calibrated every 5-10 runs; the procedure must be repeated whenever the trigger is changed, or if a long period of time elapses between runs. A five-pass system is used for these calibrations.

In the first pass, pedestal values (PED) are calculated for the ADCs attached to each photmultiplier tube in CX and the three hodoscopes. The difference between the raw ADC value (ADC_{raw}) and the pedestal yields a true ADC value ($ADC_{true} = ADC_{raw} - PED$). For each slat, a crude TOF offset (TOF) is calculated.

Slewing constants are calculated in the second pass, and further refined in the third. The TDC response of the hodoscope slats depends on the amount of charge deposited in the slat. The discrimator on the TDC needs a minimum charge to be deposited, and a large amount of charge can satisfy this threshold in a shorter length of time, so the corresponding time measurement would seem shorter. The slewing constants (SLW) are used to eliminate this dependence. The corrected TDC values

(TDC_{corr}) are calculated from the raw values (TDC_{raw}) using the following equation [Lee93]:

$$TDC_{corr} = TDC_{raw} - SLW \times \frac{1}{\sqrt{ADC_{true}}}. \tag{4.1}$$

In the fourth pass, the calibrations are completed with the calculation of several new constants, using the constants from the previous passes. First the TOF distribution is calculated. A typical TOF distribution has two peaks (for these data, one for kaons and one for protons). One of these peaks is chosen, fit to a Gaussian, and adjusted to be centered at the origin. The amount by which the peak is moved is known as the TOF offset. The y_{offset} is also calculated, the vertical position in each hodoscope slat where the two phototubes fire simultaneously. The last constants determined are the ADC gains of each photomultiplier tube (for all hodoscopes and CX), for gain matching.

The final pass is purely diagnostic in nature. The results from the previous four runs are checked, and once all the constants are deemed valid, they are inserted into the NA44 database.

4.3 Reconstruction and DST production

The next step after calibrations is the reconstruction of tracks and the production of data summary tapes (DSTs). Only some of the raw data on the IBM tapes are used in reconstruction. From the information from the hodoscopes, the strip chambers, and the pad chamber, it is determined which hits can be considered valid. These valid hits are then used to determine tracks, and the corresponding momentum for each track is calculated. All of this information is then stored in the final DST as an ntuple [Bru88].

Using the calibration constants previously calculated, the hodoscope ADC and TDC values on the tape are converted to positions in x and y (z is determined by the position of the detector) and TOF information associated with each track. To reduce noise, a hit in the hodoscopes is considered valid if its ADC value is above a minimum threshold. This prevents the reconstruction of tracks from "garbage" hits, so-called ghost tracks.

The SC and PC information is handled differently. The ADC values are pedestal subtracted before the data is saved to tape. A valid hit in these chambers appears as a cluster of pads that have fired. A deconvolution algorithm is used to identify the clusters [Spe94]. A Gaussian fit is used on the clusters (1-dimensional for the SC, 2-dimensional for the PC), and the center of the Gaussian is considered the hit position. Again, to eliminate garbage hits, a minimum ADC value is required.

A chi-squared fitting technique is used to determine tracks from the list of valid hits. Tracks are required to follow a straight line trajectory. The detector resolution is accounted for, as is the multiple scattering a particle would encounter before hitting each detector. The requirements for each track are valid hits in H2, H3, the PC, and 3 of 4 of the SC planes; H4 is not used in the reconstruction. In events with multiple tracks, a minimum distance is required between the two tracks in the PC and the SC, and tracks passing through adjacent hodoscope slats are disallowed.

Once a track is deemed valid, its momentum must be calculated. The important information here is the position of the track in the PC and in H2. A polynomial parametrization is used with the raw position of the track in the PC, but the fitted position in H2. This was found to improve the momentum resolution due to the increased multiple scattering after the PC, the closest detector to the target.

After the tracks have been fit and their momenta calculated, other track-specific information is calculated. From TOF measurements from each hodoscope, the mass-squared information for each track can be determined. Three rapidities for each track are also calculated, treating the particle as a pion, a kaon, and a proton. All this track-by-track information is written to a DST file, together with scaler information that is useful on an event-by-event basis. This includes such things as the number of ADC channels that fired in the Cerekov detectors, and the counts in each of the four sectors of the T0.

4.4 Pair Files

For the HBT analysis, the data are further reduced and simplified. Cuts are applied so that only events with multiple tracks of a given particle remain. Double beam events are eliminated with a cut on the Cerenkov beam counter ADC levels, and beam halo events are taken care of using the data from the CX veto detectors. Since most pions and electrons were removed at the trigger level with a veto on the second Cerenkov detector, a modest C2 cut is required on the data. A cut on C1 is used to differentiate between events with kaons and events with protons.

The next step is to eliminate tracks with poor quality. Tracks with a low confidence level are rejected. Since the number of particles passing through the experiment tends to be greater near the middle of the acceptance, the statistics for calibration are much lower near the edges. Therefore, a cut is made that eliminates tracks passing through the outer slats on the hodoscopes.

For final PID, TOF and mass-squared information in H2 and H3 is used. Only a loose cut on the TOF for all the hodoscopes is made; those data are used in the

calculation for mass-squared, so nothing would be gained with strict cuts on both distributions. The mass-squared peak for kaons should be centered at 0.24 GeV^2, and for protons it should be at 0.88 GeV^2. Because the spectrometer has a finite resolution, the mass-squared distributions are somewhat Gaussian, with a width of $\approx$ 0.25 GeV^2. For kaons, the mass-squared for H3 (H3MSQ) was required to fall between -0.1 and 0.6 GeV^2, and for protons, the cut was 0.6 GeV^2 <H3MSQ<1.6 GeV^2. Figure 4.1 shows the H3MSQ distributions with the C1 cut (used for kaons), and without the C1 cut (used for protons). The estimated proton contamination in the kaon sample was $\approx$ 14%; in the proton sample, there was a kaon contamination of $\approx$ 6%.

Each event that satisfies all of the cut requirements is saved in the pair file. The event information saved includes the run number, event number, T0 ADC value, silicon pad multiplicity, Si ADC sum, and number of kaons (protons). Within each event, the kaon (proton) track information written to file includes the momentum (as a 3-dimensional vector), PC position in x and y, the slat number and y position in H2 and H3, and the number of accepted SC hits for that track.

4.5 Forming the Correlation Function

With a perfect detector, the particles which were produced as pairs could be separated from those produced as singles, and the relative distributions would be divided to form the correlation function. With a real detector, the approach usually taken is to take the measured distribution of relative momenta, and divide that by

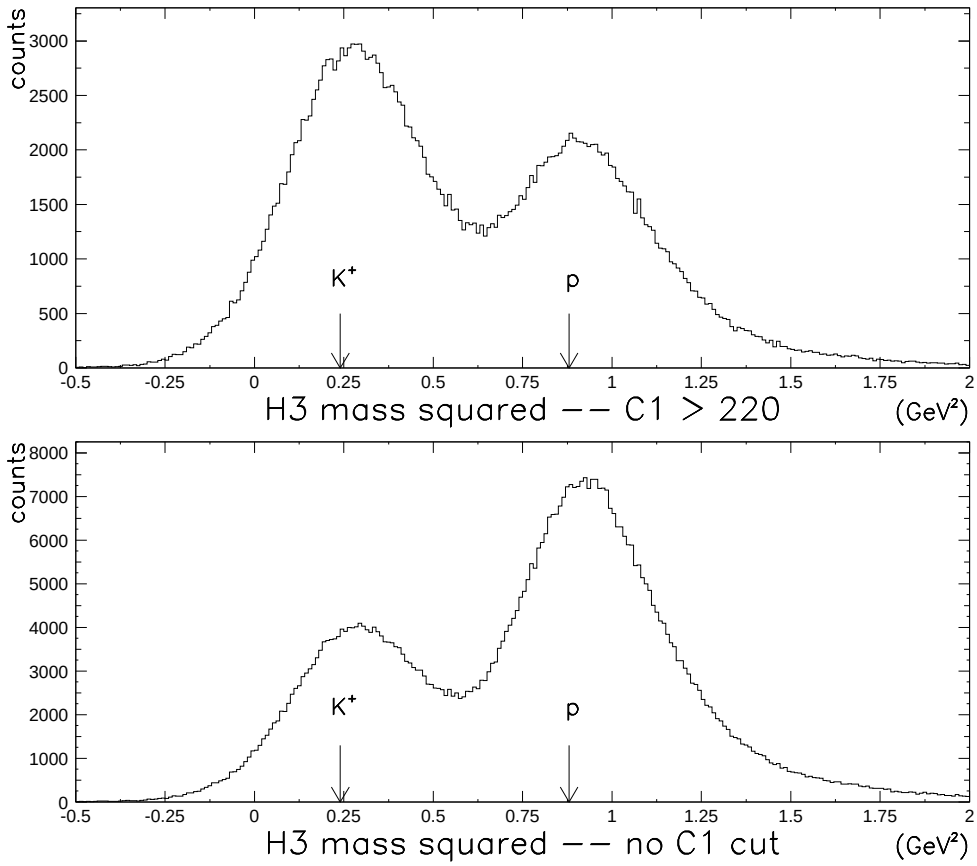

Figure 4.1: H3 mass squared distributions for the 131mr 8 GeV/c horizontal setting. The upper plot shows the distribution with events where more than 220 ADC channels in C1 fired, and the lower plot has no cut on C1. Also shown are the expected positions for the kaon and proton peaks.

a "background" distribution, one produced by mixing pairs from different events, to eliminate any non-Bose-Einstein correlations. That is, one would use the equation:

$$C_{raw}(\vec{p}_1, \vec{p}_2) = \frac{R(\vec{p}_1, \vec{p}_2)}{B(\vec{p}_1, \vec{p}_2)}, \tag{4.2}$$

where $\vec{p}_i$ are the particle momenta, $R(\vec{p}_1, \vec{p}_2)$ is the "real" distribution, and $B(\vec{p}_1, \vec{p}_2)$ is the background distribution. The background sample must be subjected to the same cuts as the real pairs. A ratio of ten background pairs to each real pair was used so the real distribution would have more influence on the statistical errors.

For protons, this raw correlation function is the final function; for kaons, various corrections are applied before a final correlation function is produced. A Coulomb correction is applied to account for the repulsion of the outgoing pair, an acceptance correction is applied to account for the experiment's finite momentum resolution and two-track efficiency, and a background correction is incorporated to eliminate effects from residual correlations from the mixed pairs. These corrections are applied on an iterative basis, so the shape of the correlation function must be known. Within 5 iterations, the results are usually quite stable.

4.5.1 Coulomb Correction

To calculate the correction due to the Coulomb interaction, the procedure outlined in Section 2.2.2 is used. One of the parameters for the Coulomb wave function integration is the size of the emitting source. The fitted values of the radius parameters from each iteration are used as the source size in the successive iteration.

The Gamow factor has also been used to correct the data, even though it is known to be less accurate than the full Coulomb wave integration. This was done to compare with the Coulomb correction.

4.5.2 Acceptance Correction

The physical limitations of the spectrometer cause several distortions to the correlation function. Since the momentum resolution is finite, there is a minimum relative momentum that can be measured, not to mention the fact that the cuts designed to eliminate ghost tracks also eliminate pairs of tracks with low relative momentum. As a result, the low relative momentum region is under-populated. Another problem arises through the Coulomb correction; this correction is applied using the measured momentum of each particle, not the particle's true momentum.

The NA44 Monte-Carlo was used to calculate the acceptance correction. Two particle events are produced with momenta $(\vec{p}_1, \vec{p}_2)$ that would pass them through the detector's acceptance. A simulated measurement is performed, yielding reconstructed momenta $(\vec{p}_1', \vec{p}_2')$. These momenta are then used to form an ideal correlation function $(C_2(ideal))$ and a reconstructed correlation function $(C_2(reconstructed))$. These are both produced in a manner similar to that for producing the raw correlation function from the data: a "real" distribution of the relative momenta is divided by a "background" distribution, or:

$$C_2(ideal) = \frac{R(\vec{p}_1, \vec{p}_2)}{B(\vec{p}_1, \vec{p}_2)}, and \tag{4.3}$$

$$C_2(reconstructed) = \frac{R(\vec{p}_1', \vec{p}_2')}{B(\vec{p}_1', \vec{p}_2')}. \tag{4.4}$$

The simulated background distribution is formed directly from the simulated momenta. The real distribution also uses the momenta, but it is weighted by the Bose-Einstein correlation. The correlation function is taken from the fit to the data. In equation form:

$$R(\vec{p}_1, \vec{p}_2) = \frac{d^6 N}{d^3\vec{p}_1\, d^3\vec{p}_2} \times C_2(\vec{p}_1, \vec{p}_2). \tag{4.5}$$

It should be pointed out that for the simulated data, there are no cuts applied to either the real distribution or the background distribution.

For the reconstructed distributions, the method is similar. The real distribution is weighted by the Bose-Einstein correlation, again taken from the data, but the function is evaluated at the *simulated* momentum points:

$$R(\vec{p}_1', \vec{p}_2') = \frac{d^6 N}{d^3\vec{p}_1'\, d^3\vec{p}_2'} \times C_2(\vec{p}_1, \vec{p}_2). \tag{4.6}$$

The background to the reconstructed correlation function is formed from mixed events, but there is an additional weighting factor to account for the misapplication of the Coulomb correction. As previously mentioned, the Coulomb correction is applied to the measured, not the actual, momenta, so the raw background distribution is scaled:

$$B(\vec{p}_1', \vec{p}_2') = B_{raw}(\vec{p}_1', \vec{p}_2') \times \frac{K_{coul}(\vec{p}_1, \vec{p}_2)}{K_{coul}(\vec{p}_1', \vec{p}_2')}, \tag{4.7}$$

where $K_{coul}(\vec{p}_1, \vec{p}_2)$ is the Coulomb correction particles with momenta $\vec{p}_1$ and $\vec{p}_2$. For the reconstructed distributions, the same cuts are applied as are applied to the data. Since both the ideal and the reconstructed distributions depend on the function fit from the data, the acceptance correction is also calculated on an iterative basis.

Once these two correlation functions are calculated, the acceptance correction factor is just the ratio between them, or:

$$K_{acc}(\vec{p}_1, \vec{p}_2) = \frac{C_2(ideal)}{C_2(reconstructed)}. \tag{4.8}$$

Figure 4.2 shows one-dimensional examples of these functions. The top plot is an ideal Monte-Carlo correlation function, the middle plot a reconstructed correlation function, and the third plot is the acceptance correction.

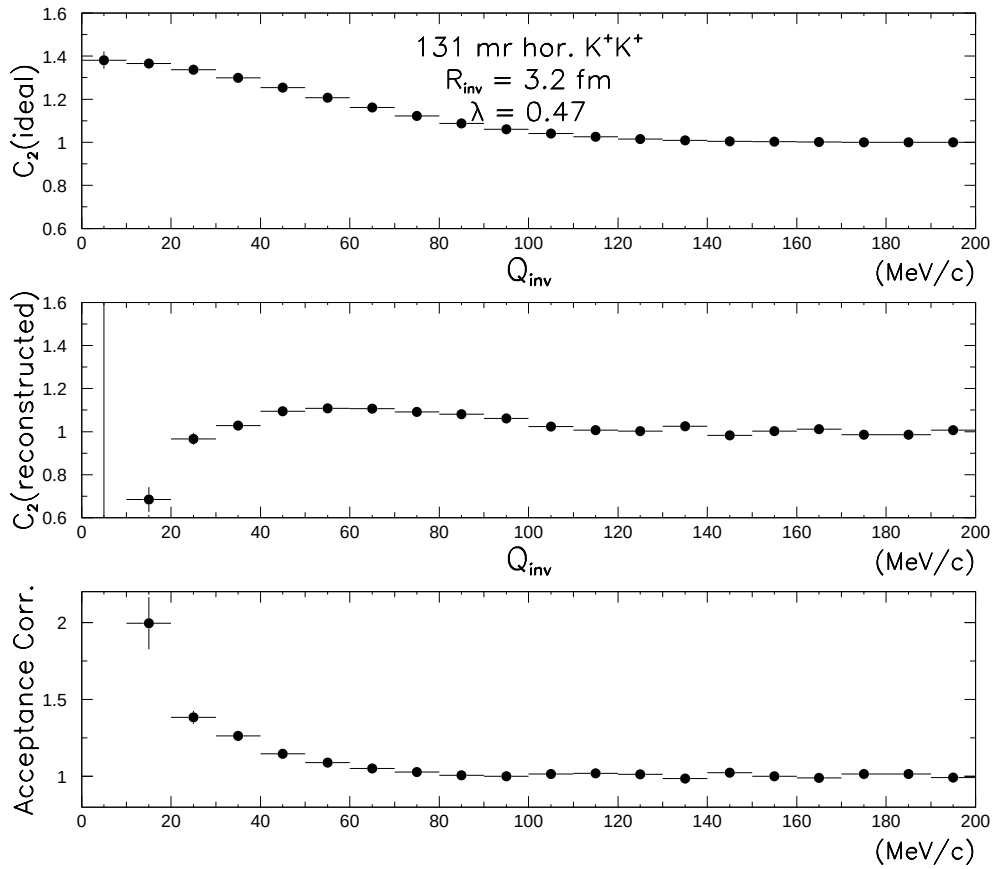

Figure 4.2: The ideal MC correlation function ($C_2(ideal)$), reconstructed MC correlation function ($C_2(reconstructed)$) and acceptance correction for kaons. The Bose-Einstein weights for each pair are calculated using $R_{inv} = 2.8$ fm and $\lambda = 0.4$.

4.5.3 Background Correction

Because the background distribution used in Equation 4.2 is generated from particle pairs from different events, it was assumed that there were no Bose-Einstein correlations between the particles. This is not necessarily a valid assumption. Zajc has shown [Zaj84] that residual correlations remain in a mixed-pair background, and Peitzmann has shown [Pei93] that these correlations are inversely proportional to the size of an experiment's acceptance. As NA44's acceptance is rather small, these residual correlations could be significant.

As with the other correction factors, in order to calculate the background correction, a functional form of the correlation must be assumed, and to further refine the correction, an iterative approach is used. The procedure used on these data was first described in [Bog93]. For the first iteration, an initial single-particle background spectrum is calculated from:

$$B^0(\vec{p}_1) = \sum_{\vec{p}_2} R(\vec{p}_1, \vec{p}_2), \tag{4.9}$$

where $R(\vec{p}_1, \vec{p}_2)$ is the numerator from Equation 4.2. For the ith iteration, the background is calculated from:

$$B^i(\vec{p}_1) = \sum_{\vec{p}_2} \frac{R(\vec{p}_1, \vec{p}_2)}{C^{i-1}_{fit}(\vec{p}_1, \vec{p}_2)}, \tag{4.10}$$

where $C^{i-1}_{fit}(\vec{p}_1, \vec{p}_2)$ is the fitted correlation function from the $(i-1)^{th}$ iteration. A background for particle-pairs is calculated from the product of two single-particle spectra:

$$B^i(\vec{p}_1, \vec{p}_2) = B^i(\vec{p}_1) B^i(\vec{p}_2). \tag{4.11}$$

From this, the background correction factor for the ith iteration is:

$$K^i_{back}(\vec{p}_1, \vec{p}_2) = \frac{B^0(\vec{p}_1, \vec{p}_2)}{B^i(\vec{p}_1, \vec{p}_2)}. \tag{4.12}$$

4.5.4 Fully Corrected Correlation Function

Once all the corrections have been calculated, the fully corrected correlation function is calculated from:

$$C_2(Q) = C_{raw}(Q) \times K_{coul} \times K_{acc} \times K_{back}, \tag{4.13}$$

where Q is the relative momentum (Q_{inv} for 1-dimensional fits, $\vec{Q}$ for higher-dimensions). It should be pointed out that each of the correctional factors required the form of the correlation to be known beforehand, so there the final correlation function has significant model dependence. However, at the present time, there exists no way to calculate the acceptance and background corrections without assuming a form to the correlation. While the initial choice of a Gaussian form may have been for simplicity, the χ^2/DOF obtained from the fits are reasonable enough to suggest this choice is a valid one.

4.6 Fitting the Correlation Function

To fit the correlation function, the MINUIT fitting package [MIN92] is used. The maximum likelihood fitting method is used for the results presented here; a chi-squared minimization technique was also used. A description of the two methods is in order.

The maximum likelihood method starts with the assumption that the data points follow Poisson statistics. This means that the probability density function would look like:

$$P(R_i|\bar{R}_i) = \frac{\bar{R}_i^{R_i}}{R_i!}e^{-\bar{R}_i}, \tag{4.14}$$

where R_i is the number of real counts in the ith bin, and $\bar{R}_i = C_i B_i$ is the expected number of counts in that bin, given C_i is the value of the function, and B_i is the number of background counts. This method assumes that the statistical errors in the background are insignificant compared to the real distribution, a reasonable assumption since there are ten times more mixed than real pairs. For all the data points, the likelihood function is the product of Equation 4.14 over all i:

$$L = \prod_i P(R_i|\bar{R}_i). \tag{4.15}$$

To reduce the roundoff error from the multiplication of many small numbers, MINUIT minimizes the logarithm of this equation:

$$-ln(L) = \sum_i \bar{R}_i - R_i ln(\bar{R}_i) + ln(R_i!). \tag{4.16}$$

The chi-squared minimization technique begins with a different function that must be minimized:

$$\chi^2 = \sum_{i,j}(C_i - R_i/B_i)V_{ij}^{-1}(C_j - R_j/B_j). \tag{4.17}$$

Here, R_i, B_i, and C_i represent the same quantities as before, and V_{ij} is a covariance matrix. If the statistical errors are uncorrelated, this expression reduces to the method of least squares:

$$\chi^2 = \sum_i \frac{(C_i - R_i/B_i)^2}{\sigma_i^2}, \tag{4.18}$$

where σ_i is the approximate error on R_i/B_i. This method is problematic for bins with limited statistics, in that σ_i could severely underestimate the true error [Pan93]. This would lead low-statistics bins to drive the fit too strongly, which is particularly troublesome in the low Q region, since the first few bins have the greatest influence on the fit.

For the results presented here, the maximum likelihood fit method was used, due to the relatively low number of kaon pairs. The chi-squared minimization technique was explored, and the results were similar. The calculation of systematic errors was then performed by hand, the details of which can be found in Appendix B.

CHAPTER 5

EXPERIMENTAL RESULTS AND DISCUSSION

In this chapter, the one-dimensional and two-dimensional results from the 131mr 8GeV Pb+Pb $\rightarrow K^+K^+ + X$ data, and preliminary one-dimensional results from the 131mr 8GeV Pb+Pb $\rightarrow pp + X$ data will be presented. A simple Gaussian source model will be used to interpret the pp results. Results from a rescattering model will be compared to the K^+K^+ data. The K^+K^+ data will be compared to an independently analyzed 44mr 6GeV data sample. All of these results will be compared to results from NA44 pion interferometry Pb+Pb collisions, as well as analysis from S+Pb collisions.

5.1 One-Dimensional K^+K^+ Correlation Functions

As stated in Section 2.3.1, the equation used in fitting the 1-dimensional correlation function is:

$$C_2(Q_{inv}) = 1 + \lambda e^{-Q_{inv}^2 R_{inv}^2}, \tag{5.1}$$

where Q_{inv} is the Lorentz invariant length of each pair's relative momentum. The one-dimensional fit to the K^+K^+ correlation functions is shown in Figure 5.1. This function has had the full Coulomb wave correction applied. Since the systematic

errors were not included in the fit, the error bars are purely statistical, as will be the case for all plots presented. With the 131mr 8GeV setting, the average transverse momentum is $< p_t > \; = \; 910$ MeV.

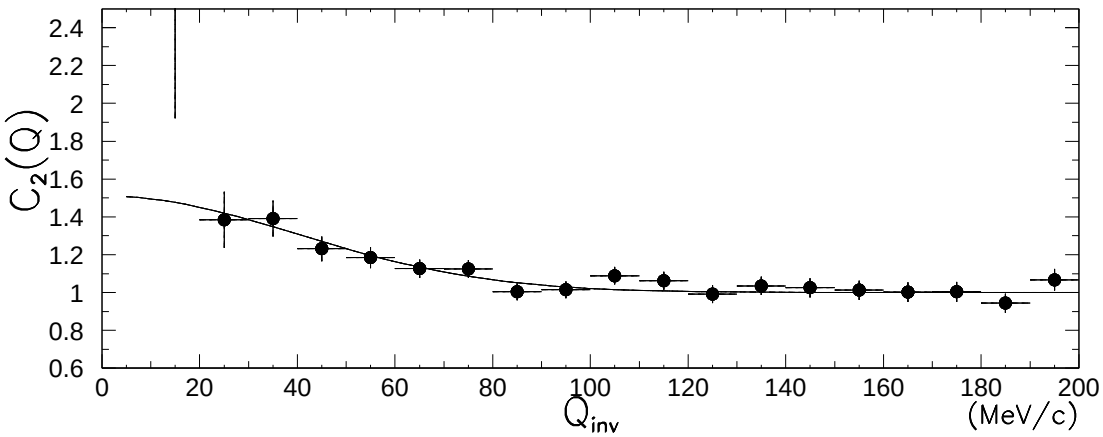

Figure 5.1: The kaon correlation function in Q_{inv}, with the full Coulomb wave correction. The solid line is the fit function.

A comparison of the Coulomb wave correction and the Gamow correction is shown in Figure 5.2. From this plot, it can clearly be seen that the Gamow corrected function is larger at low relative momentum, corresponding to a larger radius parameter. This comes from the fact that the Gamow correction treats the particle source as pointlike. It should be pointed out that for both these fits, the first bin (0-10 MeV) is empty, and the second bin has so few statistics (and hence large error bars), that it does not contribute to the fit; all other points are included.

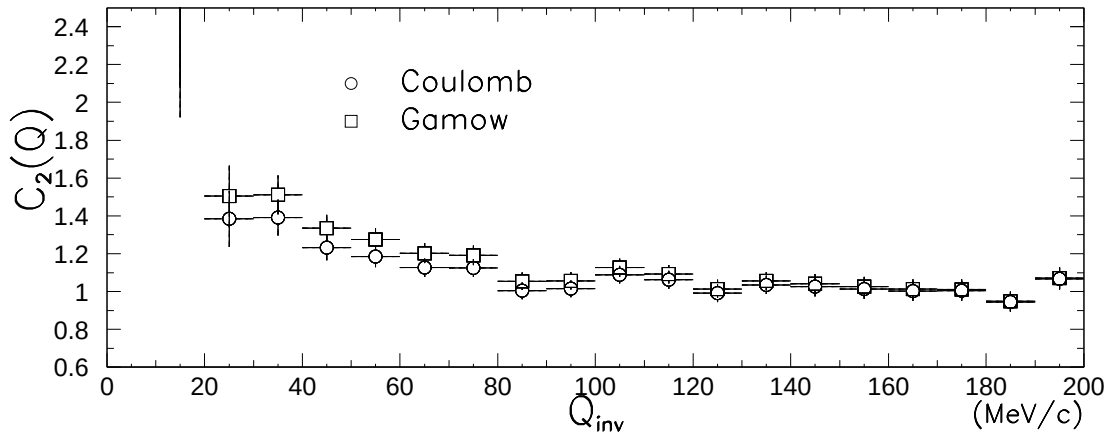

Figure 5.2: A comparison of the Coulomb Wave and Gamow corrections in Q_{inv}.

The values of the parameters from both the Coulomb and the Gamow correction correlation functions are listed in Table 5.1. The errors are listed as statistical $\pm$ systematic. Also included is the χ^2/DOF for each.

	λ	R_{inv} (fm)	χ^2/DOF
Coulomb	$0.47 \pm 0.12 \pm 0.08$	$3.28 \pm 0.62 \pm 0.75$	21/26
Gamow	$0.53 \pm 0.10 \pm 0.10$	$2.71 \pm 0.43 \pm 0.68$	23/26

Table 5.1: Fitted results of Gaussian parameterizations of the correlation function in Q_{inv}. The errors are statistical $\pm$ systematic.

The λ parameter is expected to be on the order of 1 for kaons, significantly less than that for pions. This is because pions are more likely to be produced as secondary

particles from resonances than kaons; pions from resonances would have no Bose-Einstein correlations with pions produced directly from the source. For this data sample, the reduced λ parameter is most likely a consequence of the 14% proton contamination, for which no correction was made. For each correction technique, the χ^2/DOF is on the order of unity, which implies that the assumption of a Gaussian form was reasonable.

5.2 Two-Dimensional K^+K^+ Correlation Functions

To obtain more information, more dimensions must be used in the parametrization. Ideally, a three-dimensional fit would be made, but the statistics of this kaon sample makes a two-dimensional fit the highest possible. With the Bertsch-Pratt parametrization and the LCMS reference frame, the equation used in this case is:

$$C_2(Q_T, Q_L) = 1 + \lambda e^{-Q_T^2 R_T^2 - Q_L^2 R_L^2}). \tag{5.2}$$

Projections of the Coulomb corrected function are presented in Figure 5.3. The projection in Q_L restricts Q_T to be less than 20 MeV, and the opposite is true for the other projection. The solid line represents a projection of the fit function. Figure 5.4 shows a comparison between the two different correction techniques; the Gamow correction demonstrates the same behavior as in the one-dimensional case.

Table 5.2 shows the parameters extracted from the two-dimensional fits to the correlation function, using both correction factors. Again, the χ^2/DOF for each is close to unity, indicating the validity of the Gaussian parametrization.

As in the one-dimensional fits, the Gamow correction gives smaller radius parameters than the full Coulomb Wave. Comparing the two sets of fits, one sees that λ seems larger in the two-dimensional parametrization, although, within error bars, the

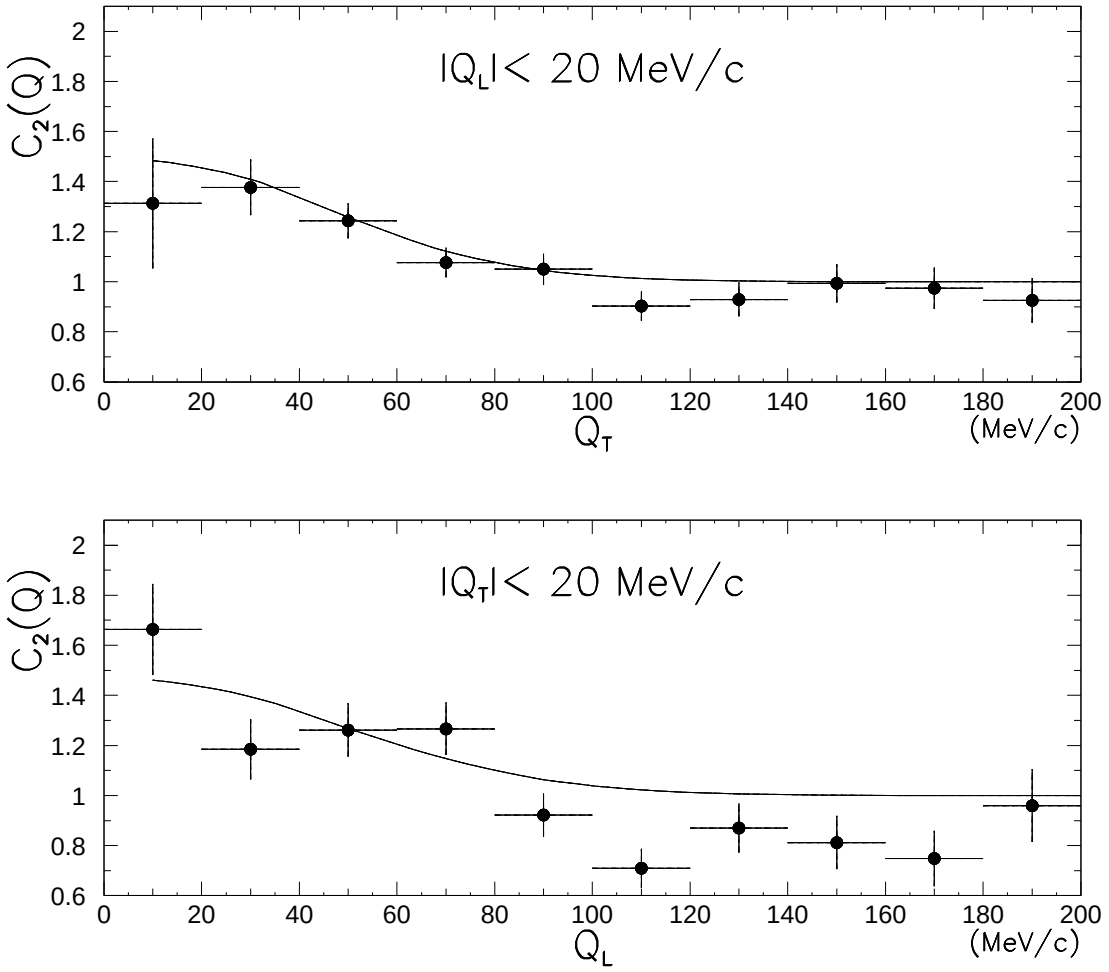

Figure 5.3: The 2d projections of the full Coulomb corrected correlation function using the standard Bertsch-Pratt parameterization.

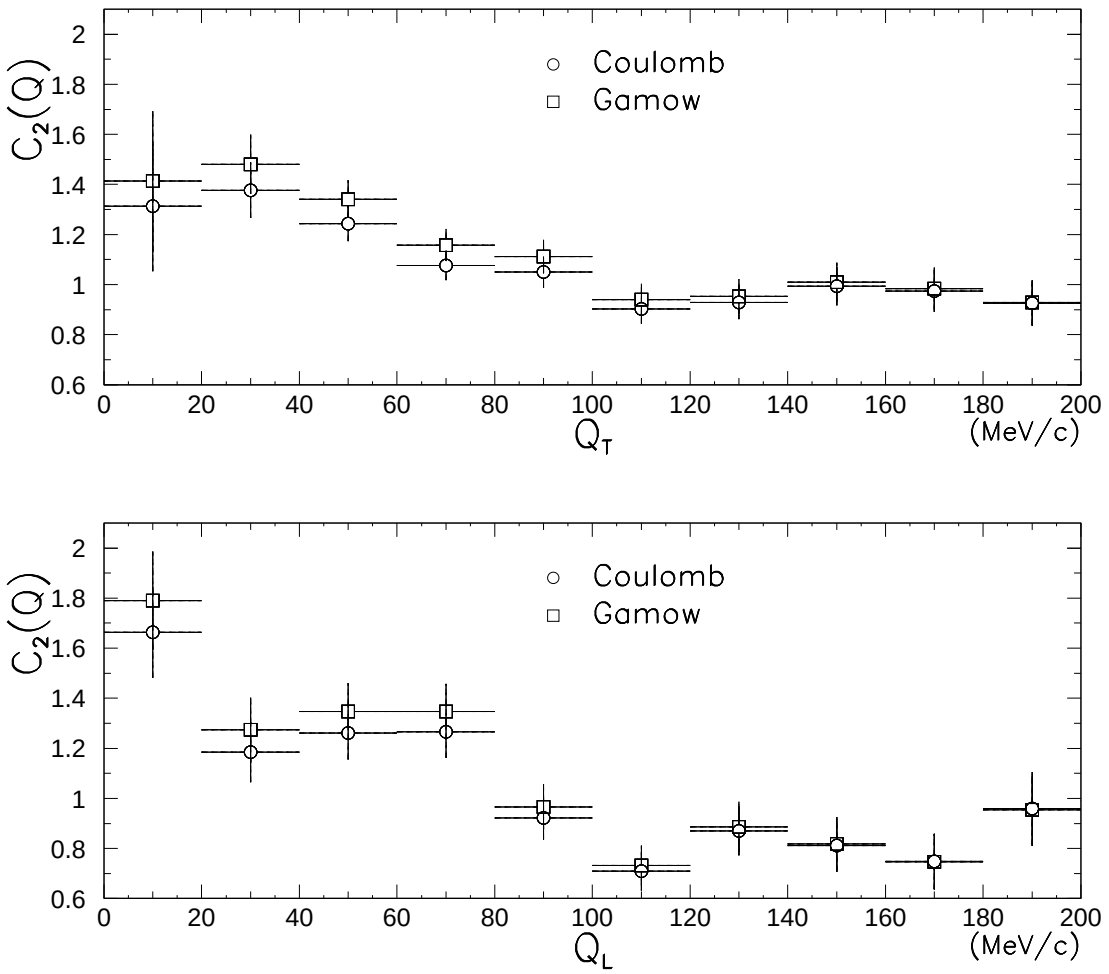

Figure 5.4: A comparison between the two different correction methods for a fit in two dimensions.

	λ	R_T (fm)	R_L (fm)	χ^2/DOF
Coulomb	0.61±0.20±0.16	3.59±0.67±0.97	3.20±0.54±0.45	117/107
Gamow	0.66±0.15±0.11	2.91±0.42±0.58	2.82±0.38±0.34	115/107

Table 5.2: Fitted results of the two-dimensional Gaussian parameterization of the correlation function with both the Coulomb wave and Gamow corrections. Errors are statistical ± systematic.

results are the same. With the radius parameters, R_{inv} seems to correspond more closely with R_L, than it does with R_T.

5.3 One-Dimensional *pp* Correlation Functions

For protons, no functional form is assumed, so no fit is made. The plot shown in Figure 5.5 is just the ratio of the real spectrum to the background, normalized so the asymptote is $y = 1$. No corrections of any kind were applied. For historical reasons, *pp* correlations are plotted with $q_{inv} = \frac{1}{2}Q_{inv}$.

To extract a radius parameter from *pp* analysis, some sort of model must be used. For this data, a simple Gaussian model was used. Random three-momentum vectors were chosen from NA44 Monte-Carlo output files, combined with random space points sampled from a Gaussian of a user-specified radius, R:

$$\rho(\vec{r}, t) = \delta(t)e^{-(\frac{1}{2}\frac{r^2}{R^2})}. \tag{5.3}$$

These points were then used as input for Pratt's Correlation After-Burner (CRAB) code [Pra94]. The output from this program for radii of 2.5 and 4.0 fm is shown in Figure 5.6.

Ten different radii were used over the range 3.0 to 4.0 fm, and a χ^2 comparison done between the generated functions and the data. The best value for R extracted

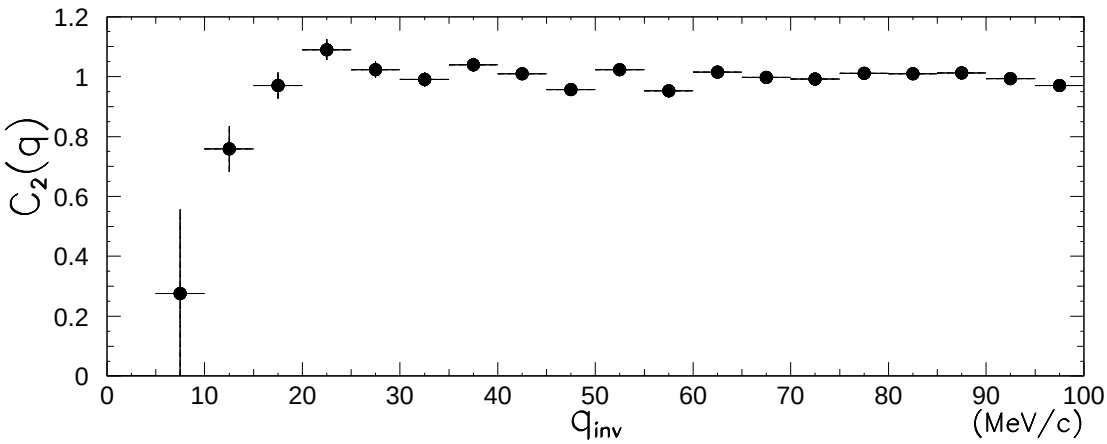

Figure 5.5: The raw correlation function for protons. Note that $q_{inv} = \frac{1}{2}Q_{inv}$.

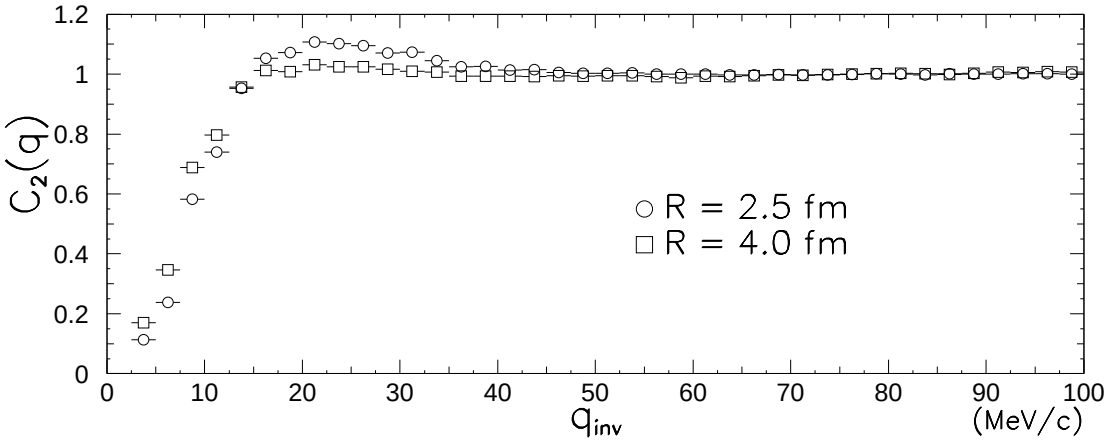

Figure 5.6: Output from the CRAB program for input Gaussian radii of 2.5 and 4.0 fm.

from this is R = 3.42 ± 0.24 fm, where the errors are purely statistical. A comparison of the data with the CRAB output for this radius is shown in Figure 5.7.

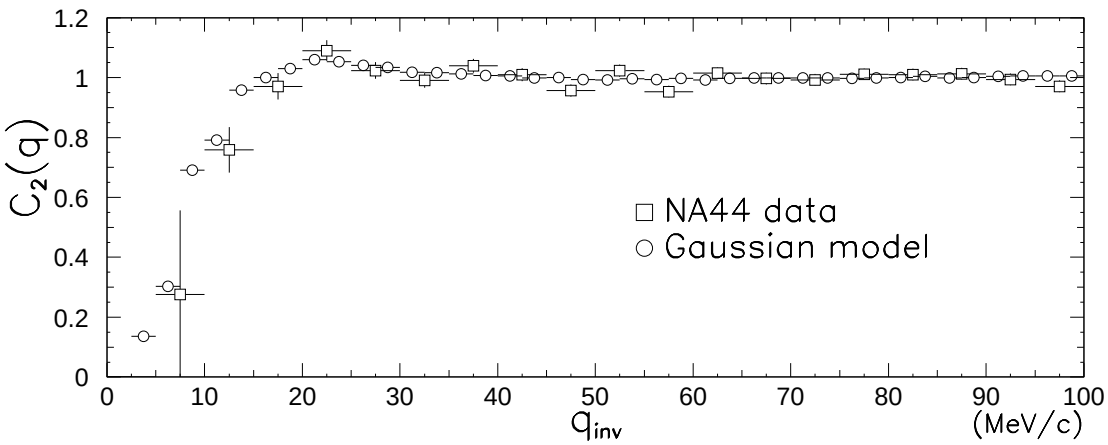

Figure 5.7: A comparison of the measured *pp* correlation function with the output from CRAB using a Gaussian source with R = 3.42 fm.

5.4 Comparison with Other Pb+Pb Interferometry Data

From 1994 through 1996, NA44 took samples of kaon and pion pairs using multiple settings. In addition to the kaon study presented here, there was also a larger sample taken in 1995 at the 44mr 6GeV setting ($< p_t > \; = \; 250$ MeV) [Bea01]. In 1994 and 1995, pion samples were taken at 44mr 4GeV ($< p_t > \; = \; 150$ MeV)and 131mr 4GeV ($< p_t > \; = \; 450$ MeV) [Bea98]. Similar analysis to that presented in this work were performed on all these samples, although there were sufficient particle pairs in all of them to enable a three-dimensional fit.

The one-dimensional and three-dimensional results for all of these analyses are listed in Table 5.3. All of these results have had the full Coulomb wave correction applied. For the kaons, the errors are listed as statistical ± systematic, while for the pions, the two errors have been combined.

System	λ	R_{inv} (fm)	χ^2/DOF
44mr K^+K^+	0.55 ± 0.09 ± 0.17	5.09 ± 0.44 ± 0.37	33/37
44mr $\pi^+\pi^+$	0.503 ± 0.046	6.66 ± 0.41	39/26
131mr $\pi^+\pi^+$	0.407 ± 0.031	5.39 ± 0.36	51/35

System	λ	R_{TO} (fm)	R_{TS} (fm)	R_L (fm)
44mr K^+K^+	0.84±0.06±0.14	4.12±0.26±0.32	4.04±0.28±0.47	4.36±0.33±0.43
44mr $\pi^+\pi^+$	0.569 ± 0.035	5.50 ± 0.26	5.87 ± 0.58	6.53 ± 0.48
131mr $\pi^+\pi^+$	0.679 ± 0.034	4.39 ± 0.18	4.39 ± 0.31	3.96 ± 0.23

System	χ^2/DOF
44mr K^+K^+	5139/2978
44mr $\pi^+\pi^+$	1423/1720
131mr $\pi^+\pi^+$	1125/1574

Table 5.3: One- and three-dimensional results from other NA44 analyses. The spectrometer setting for the kaon data was 6GeV; for the pions it was 4GeV. Errors are statistical ± systematic for kaons, statistical+systematic for pions.

A comparison of the λ parameters is only valid within the same particle species. For the kaons, the low-p_t three-dimensional λ is consistent with unity (expected for an incoherent source) and the two-dimensional result from the high-p_t sample, mostly due to the large error bars. The one-dimensional λ, while not consistent with unity, does agree with the high-p_t result, within errors. For a discussion of the $\pi^+\pi^+$ results, see [Bea98].

In order to compare the two-dimensional with the three-dimensional results, it must be pointed out that in NA44's horizontal setting, Q_T points almost exclusively in the Q_{TO} direction, so R_{TS} will be largely ignored for the following discussion. The

same trend in p_t is observed in the radius parameters for K^+K^+ as for the same parameters in $\pi^+\pi^+$; they all decrease with increasing p_t. The results from all four samples seem to show a similar trend in R_L, but not in R_{inv} or R_{TO}. A more useful comparison would be with respect to the transverse mass, m_t. Table 5.4 lists the mean p_t and m_t for all of the meson analyses. For these results, R_{inv} and R_{TO} decrease with increasing m_t. In fact, the low-p_t kaon results agree remarkably well with the high-p_t pion results, which have essentially the same average m_t. This behavior with increasing m_t has been predicted by models [Hum98].

System	$< p_t >$ (MeV)	$< m_t >$ (MeV)
44mr $\pi^+\pi^+$	150	200
131mr $\pi^+\pi^+$	450	510
44mr K^+K^+	250	550
131mr K^+K^+	910	1040

Table 5.4: Mean p_t and m_t for the different meson analyses.

5.5 Comparison to NA44 S+Pb Results

Prior to the 1994 Pb upgrade of the CERN SPS accelerator, the largest projectile nucleus available was S, with an atomic mass of 32. A sample of kaon pairs was collected using a S beam at 200 GeV and a Pb target, with the 44mr 6GeV spectrometer setting [Bek94]. The one-dimensional and three-dimensional results are listed in Table 5.5.

While the results agree within error bars with the K^+K^+ sample analyzed here, the two samples do not have the same p_t. A comparison with the low-p_t sample shows

λ	R_{inv} (fm)	χ^2/DOF
0.98 ± 0.06 ± 0.16	3.34 ± 0.16 ± 0.34	54/36

λ	R_{TO} (fm)	R_{TS} (fm)	R_L (fm)	χ^2/DOF
0.76±0.07±0.07	2.99±0.20±0.10	2.69±0.31±0.16	3.30±0.32±0.17	2404/1981

Table 5.5: One- and three-dimensional K^+K^+ results from NA44's S+Pb data. Errors are statistical ± systematic.

that at the same p_t, larger radius parameters are associated with the larger projectile. For a nucleus of atomic mass A, the Gaussian radius is given by:

$$R_{Gauss} \simeq \frac{1.2\sqrt[3]{A}}{\sqrt{5}}. \tag{5.4}$$

So for lead, $R_{Gauss} = 3.2$ fm, and for sulphur, $R_{Gauss} = 1.7$ fm, which makes the R_{Gauss} ratio of Pb to S: 1.9. The R_{inv} ratio of Pb to S is 1.5 ± 0.7, and the R_L ratio is 1.3 ± 0.7. So within error bars, the radius parameters scale with projectile ratio for K^+K^+, in contrast with $\pi^+\pi^+$, where the radius parameters increased by 5% with the larger projectile [Har97].

The S+Pb analysis for pion interferometry [Bek95] explored the dependence of the radius parameters upon the transverse mass, m_t. Specifically, these studies showed: $R_L \propto (\sqrt{m_t})^{-1}$. A plot of the radius parameters from NA44 Pb+Pb data is shown in figure 5.8. The closed points are pion data, and the open points are kaon data, except for the proton point, which is labeled. R_L and R_{pp} were then fit to the function:

$$R_L = \frac{A}{m_t^B}, \tag{5.5}$$

where A and B were the parameters for the fit. The function plotted has $A = 3.63 \pm 0.94$ and $B = 0.292 \pm 0.042$, and the reliability of the fit is shown with $\chi^2/DOF = 2.57/4$. So for Pb+Pb collisions, the relationship is closer to: $R_L \propto (\sqrt[3]{m_t})^{-1}$.

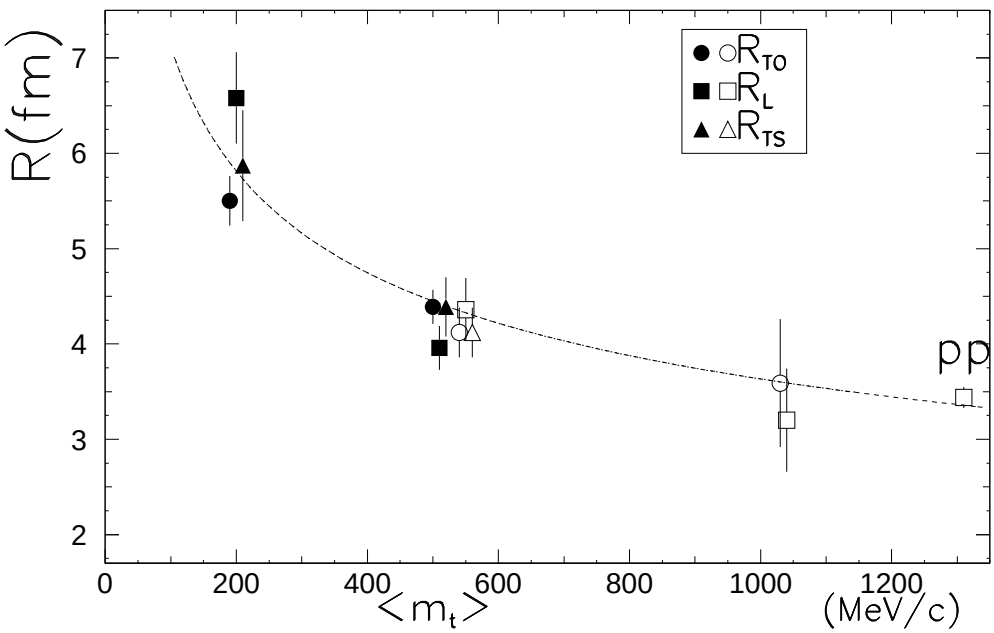

Figure 5.8: The radius parameters plotted with respect to m_t. The closed points are pion data, and the open points are kaon data, except the labeled proton point. The curve is the best fit to $R_L = Am_t^{-B}$, where A and B are fit parameters.

5.6 Comparison with a Rescattering Model

As discussed in Chapter 1, hadronic observables only probe the state of the colliding system at freeze-out, so models must be used to try and interpret the stages of the colliding system prior to freeze-out. A rescattering model [Hum94, Hum96, Hum98]

was developed in an attempt to recreate the hadronic gas stage where the particles rescatter, but have not yet experienced freeze-out.

The time prior to hadronization in this model is considered unknown and unknowable. The initial momenta are sampled from experimentally measured p_t and y distributions. The inverse slope parameter (see App. A), T, is given by:

$$T = T_{init} + m\beta_{init}^2, \tag{5.6}$$

where m is the particle mass. The inside-outside cascade model is used to determine the longitudinal hadronization position (z_{had}) and time (t_{had}):

$$z_{had} = \tau_{had} sinh(y) \tag{5.7}$$

$$t_{had} = \tau_{had} cosh(y), \tag{5.8}$$

where τ_{had} is the hadronization proper time, and y is the particle's rapidity. The free parameters for this model are T_{init}, β_{init}, σ_y, and τ_{had}, where σ_y is the width in the rapidity distribution. A comparison with experimental m_t, multiplicity, and y distributions, leads all of these parameters to be the same for all particles. Only strong interactions are considered, so positive and negative particles are treated identically, and protons and neutrons are just considered to be nucleons, N. The four lightest long-lived hadrons are included (π, K, N, and Λ) as well as several resonances (ρ, ω, η, η', ϕ, Δ, and K^*).

Once the initial conditions for the particles are calculated, the system evolves in time (with $\delta t = 0.1$ fm/c), allowing for particle decay, particle collisions and scattering, and the creation of resonances. When the system reaches a point where no more interactions occur, freeze-out is assumed, short-lived resonances are allowed to decay,

and the final space- and momentum-points are saved. From this output, two-particle correlation functions were calculated and fit using the Bertsch-Pratt parametrization.

The results from this model using a $\tau_{had} = 1$ fm/c are listed in Table 5.6 [Hum00]; the NA44 two-dimensional results are included. The calculation for these results assumed a Pb+Pb colliding system, and the transverse momentum of the final state kaons was restricted to: 600 MeV $< p_t <$ 1650 MeV.

	λ	R_{TO} (fm)	R_{TS} (fm)	R_L (fm)
Model	0.88±0.03	3.97±0.17	3.41±0.13	3.46±0.12
131mr K^+K^+	0.61±0.20±0.16	3.59±0.67±0.97		3.20±0.54±0.45

Table 5.6: Results from a three-dimensional fit to a K^+K^+ correlation function using output from the rescattering model, and the NA44 two-dimensional results.

This model shows excellent agreement with the two-dimensional results from the high-p_t kaon data sample, comparing R_T to R_{TO}. The largest discrepancy appears in the λ parameter, which reflects the effect of the proton contamination in the data.

CHAPTER 6

CONCLUSIONS

Ultra-relativistic heavy ion collisions provide a way of studying matter under the most extreme limits of mass and energy density available in a laboratory. It is believed that hadronic matter under these conditions will undergo a QCD-predicted phase transition. Experiments such as NA44 explore these collisions through the measurement of hadronic observables which probe the colliding system at freeze-out. With the help of theoretical models, these observables can help with the understanding of the earlier stages of the collision.

Two-particle interferometry provides a means for indirectly measuring the spatial volume of the colliding system at freeze-out. The K^+K^+ and pp results from NA44 presented show a smaller source size than $\pi^+\pi^+$ and K^+K^+ results from lower p_t, which has been both previously observed and predicted. All the radius parameters tend to decrease with increasing transverse mass.

When compared to S+Pb results at similar collision energy, the Pb+Pb results show a larger source size. A comparison of K^+K^+ results from the same p_t indicate that the observed source size scales directly with the projectile size, contrary to the results from $\pi^+\pi^+$ interferometry. Also, the results from S+Pb show a $(\sqrt{m_t})^{-1}$ dependence, as opposed to the $(\sqrt[3]{m_t})^{-1}$ dependence seen in the Pb+Pb data.

Finally, a rescattering model was used as a comparison to the K^+K^+ data, and it was found to agree quite well with the measured results.

The first observed collisions at Brookhaven's RHIC (Relativistic Heavy Ion Collider) in the year 2000 are paving the way for continued study in this field. At the STAR experiment (Solenoidal Tracker At RHIC), analysis of K^+ and K^- pairs is under way, as well as K^0 pairs, which would be free from Coulomb effects.

APPENDIX A

KINEMATIC VARIABLES

This work follows the convention that $\hbar = c = 1$.

For NA44, as with most (if not all) accelerator experiments, the z-direction was defined as the beam axis, positive being in the direct the beam traveled. The y-direction is the vertical direction, with "up" defined as positive. The x-direction was perpendicular to these directions, with positive x towards the left when looking downstream.

A particle's total three-momentum ($\vec{p}$) is usually specified in terms of a transverse momentum, p_t, and a rapidity, y, where:

$$p_t = \sqrt{p_x^2 + p_y^2} = \sqrt{|\vec{p}|^2 - p_z^2}, and \tag{A.1}$$

$$y = \tfrac{1}{2} ln(\tfrac{E+p_z}{E-p_z}) = tanh^{-1}(\frac{p_z}{E}), \tag{A.2}$$

where E is the particle's total energy. Rapidities add like Galilean velocities; rapidity difference is a Lorentz invariant quantity. In the low rapidity limit, $y \ll 1$ (or $p_z \ll E$), $y \simeq \beta = v/c$. Without proper particle identification, $\vec{p}$ can be measured, but the total energy is not known. In this case, the pseudorapidity, η is used:

$$\eta = -ln\ tan(\frac{p_z}{2|\vec{p}|}). \tag{A.3}$$

The energy, E, and longitudinal momentum, p_z, can also be expressed as:

$$E = m_t \, cosh(y), and \tag{A.4}$$

$$p_z = m_t \, sinh(y), \tag{A.5}$$

where the transverse mass, m_t, is defined as:

$$m_t = \sqrt{m^2 + p_t^2}. \tag{A.6}$$

The collision system is often modeled as a thermal system, in which case, the single-particle spectrum can be approximated by a Boltzmann distribution:

$$\frac{1}{m_t}\frac{dN}{dm_t} \propto e^{-m_t/T}. \tag{A.7}$$

While T is similar to a temperature, its exact interpretation is not known, so it is referred to as an "inverse slope parameter."

APPENDIX B

SYSTEMATIC ERRORS

For this analysis, five parameters were varied, and the change in the fitted results was taken to be the systematic error for that parameter. Table B.1 lists the various parameters, the value used for the main analysis, and the value chosen for the systematic error study. There may be other parameters that would contribute to the systematic error, but they were not considered for this study.

MINCNT is the minimum number of counts required for any bin to be included in the fit. This is included to prevent low-statistics bins (where the error is most likely underestimated) from contributing too strongly to the fit. Because there were plenty of statistics for a 1-dimensional analysis, and just enough for a 2-dimensional analysis, MINCNT had a greater contribution to the systematic error inthe 2-d case.

Bin size is the width chosen for each bin. Again, from statistics-based arguments, the 2-d fits were more strongly influenced by this parameter than the 1-d. The standard width used for the 2-d case was, in fact, the narrowest that could be chosen for a converging fit.

PC_CUT is the minimum distance allowed in the pad chamber betwen two tracks. A similar parameter is SUM_CUT, which compares the sum of the minimum separations in PC, H2, and H3. The acceptance correction should be able to account for these effects, but the MC was not perfect in modeling the efficiency of these detectors.

T_{MC} is the inverse slope parameter used in the MC. To generate tracks, the MC selects momenta from a Boltzmann distribution A.7. The "temperature" used for this distribution is a user-defined parameter. The value of 240 MeV was chosen from single-particle analysis.

Parameter	Standard	Variation
MINCNT (2-d)	40	20
MINCNT (1-d)	100	60
bin size (2-d)	20 MeV	30 MeV
bin size (1-d)	10 MeV	15 MeV
PC_CUT	0.5 cm	2.0 cm
SUM_CUT	10 cm	12 cm
T_{MC}	240 MeV	220 MeV

Table B.1: The standard HBT cuts and the variations used in the systematic error analysis. The meaning of each cut is explained in the text. Note that only MINCNT and bin size had different values between 1-d and 2-d.

Table B.2 lists the standard parameters, and the variations they experience when the different parameters are changed. Clearly, changing the bin size has a great effect on most of the parameters. There is no explanation for the large error on λ caused by the variation in SUM_CUT.

A comparison of the relative strengths of the systematic errors is presented in Table B.3. All of them are on the order of the statistical errors, not surprising given

Case	λ_{inv}	R_{inv} (fm)	λ	R_T (fm)	R_L (fm)
Standard	0.47±0.12	3.28±0.62	0.61±0.20	3.59±0.67	3.20±0.54
MINCNT	0.48±0.11	3.20±0.60	0.59±0.13	4.07±0.85	3.24±0.60
bin size	0.52±0.13	3.71±0.68	0.65±0.16	2.85±0.53	2.84±0.45
PC_CUT	0.50±0.16	4.07±0.73	0.62±0.22	3.75±0.74	3.28±0.57
SUM_CUT	0.51±0.14	3.42±0.63	0.75±0.27	3.94±0.78	3.39±0.58
T_{MC}	0.50±0.14	3.87±0.66	0.56±0.18	3.42±0.67	3.14±0.55

Table B.2: Fitted 1-d and 2-d results for K^+K^+ correlation functions with the variations from Table B.1. The full Coulomb wave correction has been applied to these results. Errors are purely statistical.

the relatively low number of kaon pairs. The total systematic error is then calculated by adding the errors for each source in quadrature. The statistical error is not included in the total error.

Source of Error	λ_{inv}	R_{inv}	λ	R_T	R_L
Statistics	26%	19%	33%	19%	17%
MINCNT	3%	4%	5%	13%	6%
Bin size	11%	13%	7%	20%	11%
PC_CUT	2%	4%	2%	4%	3%
SUM_CUT	9%	4%	23%	10%	6%
T_{MC}	6%	18%	8%	5%	2%
Total	16%	23%	26%	27%	14%

Table B.3: The relative error from each source, and the total systematic error.

BIBLIOGRAPHY

[Bea98] I.G. Bearden *et al.* (NA44 Collaboration), Phys. Rev. **C58**, (1998) 1656.

[Bea01] I.G. Bearden *et al.* (NA44 Collaboration), to be submitted (2001).

[Bek94] H. Beker *et al.* (NA44 Collaboration), Z. Phys. **C64** (1994) 209.

[Bek95] H. Beker *et al.* (NA44 Collaboration), Phys. Rev. Lett. **74** (1995) 3340.

[BGT88] G. Bertsch, M. Gong, and M Tohyama, Phys. Rev. **C 37** (1988) 1896.

[BGJ90] D.H.Boal, C.Gelbke, B.K.Jennings, Rev. Mod. Phys. **64** (1990) 553.

[Bog93] H. Boggild *et al.* (NA44 Collaboration), Phys. Lett. **B302** (1993) 510.

[Bow85] M.G. Bowler, Z. Phys **C29** (1985) 617.

[Bow88] M.G. Bowler, Z. Phys **C39** (1988) 81.

[Bro74] K.L.Brown, and Ch. Iselin, CERN 74-2 (1974).

[Bro80] K.L.Brown, R.Rothacker, D.C.Carey, and Ch. Iselin, CERN 80-04 (1980).

[Bru88] R. Brun and D. Lienart, **HBOOK Users Guide**, CERN Program Library Y250 (1988).

[Cha88] A.D. Chacon *et al.* Phys. Rev. Lett. **60** (1988) 780.

[GGLP60] G. Goldhaber, S. Goldhaber, W. Lee, and A. Pais, Phys. Rev. **120** (1960) 300.

[GKW79] M. Gyulassy, S.K. Kaufmann, and L.W. Wilson, Phys. Rev. **C20** (1979) 2267.

[HBT56] R. Hanbury-Brown and R.Q. Twiss, Nature **178** (1956) 1046.

[Har97] D. Hardtke, **Pion Interferometry in 158 GeV/Nucleon Pb+Pb Collisions**, Ph.D. Thesis, Ohio State University (1997).

[Hum94] T.J. Humanic, Phys. Rev. **C50** (1994) 2525.

[Hum96] T.J. Humanic, Phys. Rev. **C53** (1996) 901.

[Hum98] T.J. Humanic, Phys. Rev. **C57** (1998) 866.

[Hum00] T.J. Humanic, private communication.

[Koo77] S.E. Koonin, Phys. Lett. **B70** 1977 43.

[Lee93] Y.Y. Lee, **Bose-Einstein Correlation of High Energy Heavy Ion Collision at CERN SPS**, Ph.D. Thesis, University of Pittsburgh (1993).

[MIN92] **MINUIT - Function Minimization and Error Analysis**, CERN Program Library D506 (1992).

[Pan93] S. Pandey, **Investigation of the Space-Time Evolution of the Interaction Region in Heavy Ion Collisions using Bose-Einsten Interferometry Techniques**, Ph.D. Thesis, University of Pittsburgh (1993).

[PCZ90] S. Pratt, T Csörgő, and J. Zimányi, Phys. Rev. **C42** (1990) 2646.

[Pei93] T. Peitzmann, Z. Phys. **C 59** (1993) 127.

[Pra84] S. Pratt, Phys. Rev. Lett. **53** (1984) 1219.

[Pra86] S. Pratt, Phys Rev. **D33** (1986) 1213.

[Pra86b] S. Pratt, Phys Rev. **D33** (1986) 72.

[Pra94] S. Pratt *et al.*, Nucl. Phys. **A566**, (1994) 103c.

[Rei68] R. Reid, Annals of Physics **50** (1968) 411.

[Sch68] L. Schiff, **Quantum Mechanics**, McGraw-Hill (1968).

[Spe94] M. Spegel, **Cathode Pad Chambers on the Trail of the Quark-Gluon Plasma**, Masters Thesis, Technical Univerity of Vienna (1994).

[Zaj84] W.A. Zajc *et al.*, Phys. Rev. **C29** (1984) 2173.